The RNF168 paralog RNF169 defines a new class of ubiquitylated-histone reader involved in the response to DNA damage

Julianne Kitevski-LeBlanc[1,2,3],¶, Amélie Fradet-Turcotte[5,6]¶, Predrag Kukic[7*], Marcus D. Wilson[5,8*], Guillem Portella[7], Tairan Yuwen[1,2,3], Stephanie Panier[1,5,8], Shili Duan[9,10], Marella D. Canny[4], Hugo van Ingen[11], Cheryl H. Arrowsmith[4,9,10], John L. Rubinstein[1,4,12], Michele Vendruscolo[7], Daniel Durocher[1,4,**] and Lewis E. Kay[1,2, 3, 12**]

Department of [1]Molecular Genetics, [2]Biochemistry, [3]Chemistry and [4]Medical Biophysics, University of Toronto, ON, M5S 3E1, Canada;

[5]The Lunenfeld-Tanenbaum Research Institute, Mount Sinai Hospital, 600 University Avenue, Toronto, ON, M5G 1X5, Canada;

[6]Laval University Cancer Research Center, Oncology Axis – Centre Hospitalier Universitaire de Québec Research Center – Université Laval, Hôtel-Dieu de Québec, Québec City, QC, G1R 3S3, Canada;

[7]Department of Chemistry, University of Cambridge, Cambridge CB2 1EW, United Kingdom

[8]Present address: The Francis Crick Research Institute, 1 Midland Rd, Kings Cross, London NW1 1AT

[9]Structural Genomics Consortium, University of Toronto, Toronto, Canada.

[10]Princess Margret Cancer Centre

[11]Macromolecular Biochemistry, Leiden Institute of Chemistry, Leiden University, Einsteinweg 55, Leiden, The Netherlands.

[12]Molecular Structure and Function Program, The Hospital for Sick Children Research Institute, Toronto, ON M5G 1X8, Canada.

¶, * equal contribution

**Co-corresponding authors.

Abstract

Site-specific histone ubiquitylation plays a central role in orchestrating the response to DNA double-strand breaks (DSBs). DSBs elicit a cascade of events controlled by the ubiquitin ligase RNF168, which promotes the accumulation of repair factors such as 53BP1 and BRCA1 on the chromatin flanking the break site. RNF168 also promotes its own accumulation, and that of its paralog RNF169, but how they recognize ubiquitylated chromatin is unknown. Using methyl-TROSY solution NMR spectroscopy and molecular dynamics simulations, we present an atomic resolution model of human RNF169 binding to a ubiquitylated nucleosome, and validate it by electron cryomicroscopy. We establish that RNF169 binds to ubiquitylated H2A-Lys13/Lys15 in a manner that involves its canonical ubiquitin-binding helix and a pair of arginine-rich motifs that interact with the nucleosome acidic patch. This three-pronged interaction mechanism is distinct from that by which 53BP1 binds to ubiquitylated H2A-Lys15 highlighting the diversity in site-specific recognition of ubiquitylated nucleosomes.

Introduction

Protein ubiquitylation is a versatile signal that controls a wide range of cellular functions including protein degradation, transcription, immunity, inflammation, endocytosis and DNA repair (1, 2). The covalent attachment of ubiquitin (ub), a 76 residue polypeptide, to a target protein is achieved by the sequential activity of ubiquitin-activating (E1), ubiquitin-conjugating (E2) and ubiquitin-ligating (E3) enzymes resulting in the formation of an isopeptide bond between the terminal carboxyl group of ubiquitin and an acceptor protein. Conjugated ubiquitin can be targeted for additional ubiquitylation cycles, producing polyubiquitin chains of various lengths and topologies (1). Translating the resulting ubiquitin signal into a specific cellular response typically involves interactions between ubiquitin and proteins containing ubiquitin-binding domains (UBDs) (3). UBDs, which are small (20-150 amino acids) structurally diverse protein modules that interact with ubiquitin in a non-covalent manner, have been identified in more than 150 cellular proteins (4). The specificity of UBD-ubiquitin interactions is achieved by a variety of mechanisms that can involve distinct affinities for certain linkages and lengths of ubiquitin chains, avidity through combination of UBDs, and contributions by UBD-independent sequences within a ubiquitin binding protein (3). This latter mechanism is especially prevalent during the response to DSBs where some proteins harbor one such “specificity” sequence adjacent to the UBD, termed an LR-motif or LRM (5).

The DSB response is a useful model to study ubiquitin-based signaling. In this process, DSBs elicit a complex chromatin modification cascade, illustrated in

Figure 1A, which ultimately controls DNA repair(6). The cascade begins with the phosphorylation of the C-terminal tail of histone H2AX, by the phosphatidylinositol 3-kinase-related kinase ATM and related kinases. Phosphorylated H2AX (known as γ-H2AX) is “read” by the BRCT domains of the MDC1, which is itself a target of ATM. The ubiquitin ligase RNF8 then binds ATM-phosphorylated MDC1 where, together with the E2-conjuating enzyme UBC13, it catalyzes K63-linked polyubiquitin chains on linker histone H1. These chains on H1 are recognized by the ubiquitin-dependent recruitment module 1 (UDM1) of RNF168 (Figure 1B), a second E3 ligase that plays a key function in DSB repair (7). The RNF168-UDM1 module is composed of two ubiquitin binding domains, MIU1 (motif interacting with ubiquitin) and UMI (MIU- and UIM-related ubiquitin binding motif) along with the LRM1 specificity module. RNF168 catalyzes mono-ubiquitylation of H2A/H2AX on Lys13 or Lys15 yielding H2AK13ub and H2AK15ub, respectively (8, 9). The action of RNF168 on chromatin results in the subsequent recruitment of additional DSB repair factors including 53BP1, RAP80, RAD18 and the RNF168 paralog RNF169. RNF168 also promotes its own recruitment to DSB sites via a second UDM module, UDM2, consisting of the MIU2 UBD and the LRM2 specificity motif (Figure 1B). In contrast, RNF169 only contains a functional UDM2 module (Figure 1B), explaining the strict dependence on RNF168 for its recruitment to DSB sites (5, 10, 11).

While 53BP1, RNF168, RNF169, RAP80 and RAD18 accumulate on the chromatin surrounding DSB sites in an RNF168- and ubiquitin-dependent

manner, how these factors recognize the products of RNF168 action are only beginning to emerge. 53BP1, while lacking a recognizable UBD, specifically interacts with H2AK15ub, but not with H2AK13ub, in the context of nucleosomes also containing H4 Lys20 dimethylation (12). The structural basis for the site-specific recognition of the H2AK15ub/H4K20me2 mark by 53BP1 was recently elucidated by electron cryomicroscopy (cryo-EM) (13). The resulting structure showed that a short 53BP1 peptide segment, the ubiquitin-dependent recruitment (UDR) motif, interacts with the nucleosome core particle (NCP) surface, sandwiched by a ubiquitin molecule (13). Like 53BP1, both RNF168 and RNF169 interact with ubiquitylated H2A (5), but it is not known if this interaction is selective for H2AK13/K15ub.

Here, we first establish that RNF168 and RNF169 are site-specific readers of H2AK13/K15 ubiquitylation. Then, we make use of an integrative approach to elucidate the molecular basis for the specific recruitment of RNF168/169 to DSBs by generating a structural model of the RNF169(UDM2)-ubiquitylated nucleosome complex. Central to these efforts have been methyl-TROSY NMR, which enables the study of protein complexes with aggregate molecular masses as large as 1 MDa (14-16), and replica averaged molecular dynamics simulations (17) using restraints derived from NMR and site-directed mutagenesis experiments. Our model establishes that the previously identified bipartite interaction module of RNF169 (5) is composed of a classic MIU helix that docks onto the canonical hydrophobic surface of ubiquitin, while the LRM2 region responsible for specificity is highly disordered. The LRM2 motif binds to the

acidic patch region on the nucleosome surface using two basic regions with key arginine residues. We then use cryo-EM to validate this model. These results demonstrate the synergistic behavior of MIU-ubiquitin and LRM-NCP acidic patch interactions in facilitating recruitment of histone ubiquitylation readers RNF168/RNF169 to regions of DSBs and in providing the specificity of the interaction.

Results

The RNF169 UDM2 module interacts with H2AK13/K15ub NCPs

To identify additional proteins that specifically recognize H2AK13/K15ub in the context of nucleosomes, we prepared MBP fusion proteins with the RNF168 UDM1 and UDM2 modules, the RNF169 UDM2 module and regions of RAD18 and RAP80 that are necessary and sufficient for their ubiquitin-dependent recruitment to DSB sites (5). We observed that the RNF168 and RNF169 UDM2 modules were the only proteins, among those tested, that bound to NCPs catalytically ubiquitylated with the RNF168(1-113)-UBCH5a complex in MBP pull-down assays (Figure 1C). These data suggested that the RNF168 and RNF169 UDM2 modules might represent selective readers of H2A Lys-13/Lys-15 ubiquitylation.

H2A is the most abundant ubiquitylated protein in the nucleus with 5-15% of H2A conjugated to ubiquitin at the K119 residue in vertebrate cells (18). As the BMI1-RING1b complex can catalyze this mark (19), we tested whether the RNF168 or RNF169 UDM2 modules interact with H2AK119ub-containing NCPs

prepared using the BMI1-RING1b enzyme complex. While both RNF169(UDM2) and RNF168(UDM2) were able to pull-down H2A K13/K15ub-NCPs, they were unable to interact with BMI1/RING1b-ubiquitylated NCPs (Figure 1D). Although both NCP substrates provide accessible ubiquitin molecules, since they are attached to unstructured histone tails, the ubiquitin moieties reside on opposite ends of the NCP surface (Figure 1E). Therefore, these results imply that the UDM2 module makes specific contacts with the N-terminal region of H2A or with the surrounding NCP surface, rather than non-specific interactions with DNA, to establish a strong and selective association with ubiquitylated NCPs.

Solution NMR of RNF169(UDM2) and its binding to ubiquitin and to ubiquitylated NCPs

Having identified an interaction module required for binding of H2AK13/K15ub-NCPs, involving both MIU and LRM domains, we then used solution NMR spectroscopy to establish the secondary structures of these elements in the unbound state. The primary sequences of RNF169(UDM2) and RNF168(UDM2), encompassing the MIU2 and LRM2 domains, are shown in Figure 2A. Residues 665-682 of RNF169 and 442-459 of RNF168 comprise the conserved primary sequence specific to MIUs, while the 13 residue long LRM2 regions contain the critical upstream arginine (R689 in RNF169 and R466 in RNF168) and the LR pair (L699/R700 in RNF169 and L476/R477 in RNF168) required for the stable interaction with NCPs ubiquitylated by RNF168 (5). Despite the fact that RNF168 and RNF169 have high sequence similarity within their analogous

MIU2-LRM2 modules, we observed a more robust interaction between RNF169(UDM2) and H2AK13/K15ub-NCPs in MBP pull-down experiments (Figure 1-figure supplement 1A). Consequently, we focused our NMR experiments and subsequent structural models on the RNF169(UDM2)-H2AK13ub-NCP interaction since we ascertained that the UDM2 module, unlike 53BP1, can bind to either H2AK13ub or H2AK15ub (Figure 1-figure supplement 1B) (12). Assignment of RNF169(UDM2) backbone resonances was carried out using standard triple-resonance solution NMR experiments (20) at 35°C, with the assigned ^{1}H-^{15}N HSQC spectrum shown in Figure 2B. The secondary structural propensity program SSP was used to determine the type and probability of secondary structural elements based on measured ^{1}Hα, ^{13}Cα, ^{13}Cβ, and ^{13}CO chemical shifts (21). The results, shown in Figure 2C, indicate a relatively high propensity for helical secondary structure over much of the MIU2 region (665-682) and some propensity for helix into the region linking the MIU2 and LRM2 domains (683-685). The remaining linker region, LRM2, and residues C-terminal to the LRM2 appear to lack any secondary structure, aside from a modest increase in helical propensity peaking at residues Y697 and L698, with an average 28% helical probability. These two residues are dynamic with Chemical Shift Index (CSI) based order parameters (22) of 0.56 and 0.46, respectively, where the order parameter is a metric used to quantify the amplitude of backbone motion, ranging from 0 (isotropic motion) to 1 (rigid) (23). In contrast, an average value for CSI-based order parameters of 0.80±0.04 is obtained for the MIU2 sequence, indicating that it is significantly more rigid. On the basis of

MIU2 sequence conservation and the formation of helical structure in the MIU2 region, it is likely that the MIU2 of RNF169(UDM2) interacts with ubiquitin via a classic MIU-ub interaction, whereby the helical arrangement aligns critical hydrophobic residues on one face of the helix so as to form contacts with the canonical hydrophobic patch of ubiquitin (24).

In order to improve the thermal stability of the MIU2 helix, we engineered an RNF169 protein containing the UDM2 sequence as before but where an aspartic acid, acting as a N-terminal helix cap, was introduced, followed by three alanine residues prior to K662, Figure 2A (Figure 2-figure supplement 1A). This peptide was used in all NMR studies with NCPs, since it tolerates temperatures of 45^{o}C, where spectral quality is improved. It is noteworthy that the helical content of the thermostable variant at 45°C is near that of the wild-type peptide at 35°C, as shown by circular dichroism spectroscopy (Figure 2-figure supplement 1B).

To experimentally establish the molecular basis for the interaction between the MIU2 of RNF169 and ubiquitin, we performed NMR-based titrations of isotope-labeled ubiquitin, both free and chemically-attached to reconstituted nucleosomes. Chemical ubiquitylation of H2A at position K13 was achieved by converting G76 of ubiquitin and K13 in H2A to cysteine residues followed by conjugation via a sidechain-sidechain disulfide linkage (Figure 3-figure supplement 1A). The ubiquitylated histone was then assembled into octamers and wrapped with DNA in the absence of any reducing agent to produce H2AK13Cub-NCPs, as previously described (25). The significant mass difference

213 between free ubiquitin and ubiquitin conjugated to NCPs enabled the use of
214 NMR-based ^{13}C-edited diffusion experiments (26), focusing on ubiquitin labeled
215 with $^{13}CH_3$ methyl groups (see below), to confirm the conjugation product and
216 monitor sample stability (Figure 3-figure supplement 1B). The diffusion constant
217 so obtained, D = 3.4±0.2 x10^{-7} cm^2/s at 25°C, is consistent with a particle of
218 molecular mass of approximately 250 kDa and is slightly smaller than for the 1/4
219 proteasome comprising a heptameric ring of α-subunits (180 kDa) (27) where D
220 = 4.2±0.1 x 10^{-7} cm^2/s has been measured under identical conditions. That the
221 C76ub-C13H2A sidechain disulfide linkage supports RNF169 binding was
222 demonstrated by showing that MBP-RNF169(UDM2) pulled down H2AK13Cub-
223 NCPs as efficiently as catalytically prepared H2AK13ub-NCPs containing the
224 isopeptide linkage (Figure 3-figure supplement 1C).
225 Having established both the suitability and the stability of our H2AK13Cub-
226 NCPs, we carried out NMR titration experiments with RNF169(UDM2) (unlabeled
227 RNF169 in the case of free ubiquitin and perdeuterated for NCPs) using ^{13}C-
228 labeled free ubiquitin or highly deuterated, Ile-δ□□$^{□□}$□□□, Leu,Val-$^{13}CH_3$,$^{12}CD_3$-
229 ubiquitin (referred to as ILV-methyl labeled in what follows) attached to
230 H2AK13Cub-NCPs (perdeuterated histone NCPs). Figure 3A shows a series of
231 overlaid ^{1}H-^{13}C HMQC spectra of ILV-methyl labeled ubiquitin in H2AK13Cub-
232 NCPs as a function of increasing amounts of RNF169(UDM2). Chemical shift
233 perturbations (CSPs) in both free (Figure 3-figure supplement 2A) and NCP-
234 bound ubiquitin were of the same direction and magnitude, indicating very similar
235 interactions for RNF169(UDM2) with both free and NCP-bound ubiquitin. Peaks

236 exhibiting the largest CSPs are derived from residues that contribute to the
237 canonical ubiquitin hydrophobic patch, including I44, L8 and V70 (3). Indeed,
238 NCPs conjugated to ubiquitin harboring an I44A point mutation failed to interact
239 with the UDM2 module of both RNF168 and RNF169 in MBP pull-downs (Figure
240 3-figure supplement 2B). CSP-derived binding curves were fit to extract
241 equilibrium dissociation constants for RNF169(UDM2) with free ubiquitin and
242 H2AK13Cub-NCPs of 956±340 μM, 45°C, and 24±7 μM, 45°C, respectively
243 (Figure 3B). It is noteworthy that only residues with relatively small CSPs,
244 corresponding to fast exchange on the NMR chemical shift timescale, were
245 included in the analysis since in this limit chemical shifts are directly related to
246 dissociation constants (K_D) and are not influenced by kinetics, allowing reliable
247 estimates of affinity from peak positions. The low affinity interaction between
248 RNF169(UDM2) and free ubiquitin is characteristic of ubiquitin binding domains,
249 having dissociation constants generally larger than 100 μM (28). The presence of
250 the NCP increases the affinity by approximately 40-fold, presumably through
251 specific contacts between the LRM2 and the NCP surface near K13 of H2A. The
252 use of two cooperative, relatively low affinity interactions to impart specificity is a
253 common theme of ubiquitin signaling (29).

254 Notably, for I44, that has the largest CSP upon binding (~126 Hz),
255 exchange between RNF169(UDM2) free and bound NCP states is in the
256 intermediate regime on the chemical shift timescale, facilitating the extraction of
257 kinetic parameters via lineshape analysis (30). Figure 3C shows a comparison of
258 experimental lineshapes (black) extracted from the ^{13}C dimension of ^{1}H-^{13}C

HMQC spectra for I44 (δ1 methyl) as a function of increasing amounts of added RNF169(UDM2), with fitted simulated lineshapes that include the effects of chemical exchange in red. Using the value of K_D = 24 ± 7 μM estimated from the titration data, on and off-rates are fit to be 2.4±0.7 x 10^7 M^{-1} s^{-1} and 5.4±0.4 x 10^2 s^{-1} respectively. Notably, the RNF169(UDM2) on-rate is an order of magnitude faster than the diffusion limit (31, 32), emphasizing the importance of electrostatic interactions in contributing to the association.

Methyl-TROSY NMR reveals RNF169(UDM2) binding sites on the NCP

To investigate the regions of the NCP involved in the interaction with the LRM2 we monitored CSPs in ^{1}H-^{13}C HMQC spectra upon addition of RNF169(UDM2). As discussed previously methyl-HMQC spectra are significantly enhanced in sensitivity and resolution by a methyl-TROSY effect that preserves signal (33). This aspect is of particular importance in applications to high molecular weight proteins and protein complexes (14-16), such as the NCP (34). Figure 4A shows ^{1}H-^{13}C HMQCs of ILV-methyl labeled H2A and H2B in the context of H2AK13Cub-NCPs, unbound or with saturating amounts of RNF169(UDM2). Corresponding weighted CSPs are tabulated in Figure 4B (see Materials and Methods). Upon binding RNF169(UDM2) L64δ2 of H2A and V41γ1, V45γ1, V63b, L99a and L103δ1/δ2 of H2B showed significant CSPs. Note that in the absence of stereospecific assignments isopropyl methyl groups are referred to as ‘a’ or ‘b’ to denote upfield and downfield resonating moieties. Interestingly, the methyl-bearing residues mentioned above surround a highly negative surface of the

H2A/H2B dimer, known as the acidic patch. The acidic patch is comprised of eight residues in total; six in H2A (E55(E56), E60(E61), E63(E64), D89(D90), E90(E91) and E91(E92) in *Drosophila melanogaster* (*Homo sapiens*)) and two in H2B (E102 and E110), creating a contoured and highly charged groove (35). The acidic patch is a well-characterized interaction surface for a multitude of NCP binding proteins with a broad range of functions (34, 36-40). Interestingly, no significant CSPs were observed in H3 (Figure 4-figure supplement 1), consistent with localized interactions involving the H2A/H2B dimer face of the NCP (Figure 4C).

While the methyl-TROSY NMR results implicate the acidic patch surface as the main contact point between the NCP and LRM2, we made use of a combined site-directed mutagenesis – NMR approach to directly monitor the effect of acidic patch residues. Specifically, we prepared H2AK13Cub-NCPs with pairwise mutations in H2A including D89A/E91A and E60A/E63A, effectively neutralizing two regions of the acidic patch surface. The first mutant, H2A D89A/E91A, alters a region of the acidic patch that is responsible for making several contacts with the canonical residue common to all known acidic patch binding proteins (41). The second mutant, H2A E60A/E63A, was designed to neutralize the region of the acidic patch closer to the DNA, where additional contacts have been identified in NCP binding proteins (35). The large chemical shift changes of isoleucine residues in ubiquitin upon binding RNF169(UDM2) provide spectral signatures of free and RNF169(UDM2)-bound H2AK13Cub-NCPs, enabling a straightforward comparison of the binding capacity of the H2A

mutants described above with wild-type H2A containing NCPs. The isoleucine region of ubiquitin in H2AK13C(D89A/E91A)ub- and H2AK13C(E60A/E63A)ub-NCPs, after addition of equivalent amounts of RNF169(UDM2), are shown in Figure 4D, overlaid with free (black) and RNF169(UDM2)-bound wild-type H2AK13Cub-NCP (red) spectra. For both H2AK13C(D89A/E91A)ub- and H2AK13C(E60A/E63A)ub-NCPs the binding capacity for RNF169(UDM2) is reduced considerably, with K_D values of approximately 280±100 μM and 230 ±100 μM relative to 25 μM for binding to wild-type NCPs. The compromised binding displayed by the H2A mutant-NCPs provides strong validation of the methyl-TROSY CSP data and indicates that at least one member of each pairwise H2A mutant plays an important role in the interaction. Moreover, the mutagenesis data extends the range of NCP residues that can be investigated, since the NMR analysis is limited to only methyl-containing amino acids.

Identification of key residues within the LRM2

Previous work has identified several highly conserved residues within the LRM2 of both RNF168 and RNF169 that are vital to their accumulation at DSBs (5). Individual substitutions of R689, Y697, and pairwise substitution of L699/R700 to alanine were found to abrogate recruitment of GST-RNF169(UDM2) to IR-induced foci (5). In agreement with these findings, R689A, Y697A, L699A and R700A were all found to reduce the capacity of RNF169 to inhibit 53BP1 focus formation after irradiation with a 2 Gy dose of X-rays (Figure 5-figure supplement 1).

While methyl-TROSY NMR was instrumental in identifying the acidic patch of the NCP surface as an important component in the interaction, a similar CSP-based analysis of the LRM2 was hampered by the presence of only 3 methyl-bearing residues in this motif (V694, L698 and L699) and by the complete resonance overlap of L698 and L699 (Figure 5-figure supplement 2). To confirm the results of the biological assay involving 53BP1 that established key LRM2 residues, we used a mutagenesis and methyl-TROSY NMR approach, similar to that described above. As before, we made use of the free and RNF169(UDM2)-bound signature spectra of isoleucine residues in ubiquitin to qualitatively evaluate the ability of single residue substitutions in RNF169(UDM2) to form a complex with wild-type H2AK13Cub-NCPs (Figure 5). As expected, R689, L699 and R700 substitutions reduce the ability of RNF169 to form a complex with H2AK13Cub-NCPs, while Y697A was also observed to impede binding to a significant degree, and S701A exhibited the smallest decrease in binding capacity.

As mentioned above, the acidic patch is a common interaction surface for nucleosome binding proteins that typically involves key contacts between an arginine sidechain and the nucleosome surface (34). The Kaposi's sarcoma herpes virus (KHSV) latency associated nuclear antigen (LANA) is an acidic patch binding protein with a critical LR-like motif (Figure 5-figure supplement 3A). MBP pull-down assays established that a LANA-derived peptide competes with RNF169 for H2AK13/K15ub-NCP binding with an estimated IC50 of 125 – 500 μM (Figure 1-figure supplement 1A) (36). However, it was not clear *a priori*

whether one or both of the basic stretches of residues in RNF169(UDM2) (R689-R690-K691 or L699-R700-S701) was important for binding and whether one mimicked the critical L8-R9-S10 sequence in LANA. A comparison of CPSs in ILV-labeled H2B upon binding RNF169(UDM2), LANA(1-23) and two RNF169(UDM2) triple mutants, (RNF169(R689A/R690A/K691A) and RNF169(L699A/R700A/S701A)), revealed similar chemical shift perturbation patterns between LANA and both RNF169 triple mutants (Figure 5-figure supplement 3B). While these results were unable to definitively identify the anchoring arginine in RNF169(UDM2), the fact that both triple mutants bound H2AK13Cub-NCPs reinforces the importance of both the RRK and LRS regions of RNF169(UDM2).

Computational modeling reveals structural details of the RNF169(UDM2) - H2AK13Cub-NCP complex

Our experimental data indicate the importance of three interactions for the selective recognition of H2AK13/K15ub-NCPs by RNF169(UDM2). The first, encompassing the MIU2 residues 665-682, is of low affinity, like for many MIU-ub complexes involving the canonical hydrophobic surface of ubiquitin (28). This weak interaction is strengthened through two additional contacts between the nucleosome acidic patch and the RRK and LRS regions of RNF169(UDM2) that provides selectivity for NCPs ubiquitylated on K13 or K15 of H2A.

As a first step to obtain the structure of the complex we docked the MIU2 region of RNF169, corresponding to residues 662-682, onto ubiquitin (PDB ID

374 1UBQ) using experimental CSPs and a number of inter-molecular nuclear
375 Overhauser effects (NOEs) as restraints (see Materials and Methods) with the
376 HADDOCK molecular modeling program (42). Methyl chemical shift changes in
377 the MIU2 region upon binding ubiquitin are localized to L672δ1/δ2, A673, and
378 L676δ1/δ2, highly conserved MIU residues that are directly involved in the
379 interaction (Figure 6A) (5, 24). Key NOEs connect A673 of the MIU2 to L8 and
380 I44 of Ub, Figure 6B. The resulting HADDOCK model is shown in Figure 6C
381 aligned with the X-ray structure of the Rabex MIU-ubiquitin complex (24). Aside
382 from a slight tilt in helix orientation (compare blue Rabex and gold RNF169
383 helices) the RNF169(665-682) MIU2-ub model is very similar to that previously
384 published for the Rabex MIU-ub complex.

385 Having elucidated the structure of the MIU2-ub component of the complex,
386 we next used cryo-EM in an attempt to obtain structural models of the ub-NCP
387 particles in both the free and RNF169-bound states. Recent advances in single
388 particle cryo-EM instrumentation and data processing have facilitated the
389 calculation of high-resolution 3D-maps of biomolecules as small as 60 kDa (43-
390 45). Figures 7A-B show cryo-EM density maps of free and RNF169-bound
391 NCPs, determined at 8.1 and 6.6 Å resolution, respectively (Figure 7-figure
392 supplement 1). In both cases the rigid NCP forms the symmetrical discoid shape
393 expected from NCP x-ray structures (46). A striking difference between the two
394 maps is the density corresponding to ubiquitin, which at the threshold level used,
395 is only visible in the RNF169-bound state. In the absence of RNF169(UDM2)
396 ubiquitin is highly dynamic, occupying a variety of positions with respect to the

NCP due to its conjugation to the flexible N-terminal tail of H2A. The density in this portion of the map is thus low in comparison to the NCP core itself. These results are illustrated in Figure 7C using equivalent lateral slices through free and RNF169-bound NCP cryo-EM maps, with the raw map density colored according to local resolution estimates (47). As expected, the NCP core in both maps exhibits the highest resolution, while the resolution of the ubiquitin region of the map is significantly lower in the absence of RNF169(UDM2). The restricted motion of ubiquitin within the complex can also be established by measuring NMR spin relaxation rates of ubiquitin methyl probes in H2AK13Cub NCPs in the presence and absence of RNF169. Here we have quantified intra-methyl ^{1}H-^{1}H dipolar cross-correlated relaxation rates (48), focusing on ILV residues. In the macromolecular limit these rates are proportional to the product $S^2\tau_C$, where S^2 is the square of an order parameter describing the amplitude of motion for the 3-fold symmetry axis of the methyl group, and τ_c is the molecular tumbling time that in the present case provides a measure for how rigidly attached ubiquitin is to the NCP. Residue specific $S^2\tau_c$ values are plotted in Figure 7D for ub-NCP (blue) and for RNF169(UDM2) ub-NCP (pink) with an average 2-fold increase, reflecting a reduction in conformational space available to ubiquitin upon addition of RNF169(UDM2).

While the cryo-EM map defined aspects of the overall topology of the complex, higher resolution information is required to obtain an atomic level description of key interactions that provide specificity and, in particular, to resolve the role of the important arginine residues, R689 and R700. We used replica-

averaged molecular dynamics simulations to develop a structural model consistent with our experimental NMR and mutagenesis data (17, 49, 50). In this method experimental data are incorporated during the simulations as replica-averaged restraints whereby back-calculated parameters are compared with their experimentally measured values to evolve the system in a manner such that the agreement with the experimental restraints increases over time. This approach is described in detail in Materials and Methods and illustrated schematically in Figure 8-figure supplement 1.

Figure 8A shows an overlay of ten members from the calculated ensemble of approximately 600 structures. Enlarged views of a pair of structures, focusing on the region of contact between the LRM2 (blue) and acidic patch residues (yellow and red), are highlighted in Figure 8B. Notably, in the great majority of structures the LRM2 backbone remains highly disordered within the complex and does not form regular secondary structure. In less than 5% of the conformers the LRM2 region contains either a small antiparallel β sheet encompassing residues Y697 to M704, or a small 3-residue helix involving residues between Y697 and M704. Importantly, in all members of the ensemble R700 is consistently located in the position where it makes contacts with one or more of the key acidic patch residues E60, D89 and E91. R689 also contacts the acidic patch in all structures through interactions involving at least one of E60 (H2A), E63 (H2A) or D48 (H2B). As shown in Figure 8B, the position of R700 within the ensemble is relatively fixed, while R689 alternates between positions that permit electrostatic contacts with E63 or D48. Although R700 and R689 were shown by mutagenesis

443 to be almost equally important for formation of the RNF169(UMD2)-ubNCP
444 complex (see above), our replica-averaged MD results indicate that R700, rather
445 than R689, is the critical anchoring arginine. Mutagenesis and NMR studies also
446 indicate a significant role for L699 and, to a lesser extent for Y697 in complex
447 formation (Figure 5A). For a significant subset of the structural ensemble
448 members, Y697 and L699 sample positions which direct their sidechains toward
449 a hydrophobic pocket formed by H2A Y49, V53 and Y56, much like the positions
450 of M6 and L8 in the LANA peptide – NCP structure (36). In addition, there are
451 alternative conformations of L699 where it appears to make no direct contact to
452 the NCP surface, but instead interacts with regions of the LRM2 module itself.
453 For example, L699 is observed to interact with M704 or A705 in some members
454 of the ensemble.

455 We have carried out further simulations to verify the important role of
456 R700 by performing a series of 50 simulated annealing cycles per replica in the
457 absence of experimental restraints and cycling the simulation temperature from
458 300K to 500K and back to 300K in each cycle (see Materials and Methods). In all
459 cases R700 remained in the canonical anchoring position in the acidic patch. As
460 a further test to examine the possibility that R689 can replace R700 in the acidic
461 patch we started from a structure in which the sidechain of R689 was forced into
462 the anchoring position and subsequently carried out a series of simulated
463 annealing cycles. After approximately 8 cycles R689 moved out of the anchoring
464 pocket and after an additional 10 cycles R700 inserted into the pocket where it
465 remained for the final 12 cycles of the simulation.

Although the resolution of the cryo-EM model (Figure 7A-C) is not sufficient to obtain atomic, insights it can be used to cross-validate some aspects of our ensemble averaged restrained MD models, in particular the location of ubiquitin. In Figure 8C, 10 replica-averaged MD derived structures are superimposed on the cryo-EM envelope and the positions of the ubiquitin molecules (magenta) fit well to the cryo-EM map. Notably, the final position of ubiquitin does not depend on its initial position in MD simulations. Figure 8-figure supplement 2A highlights a pair of H2AK13Cub-NCPs with ubiquitin in different starting positions, relative to the NCP, with convergence to similar final positions obtained in both cases (Figure 8-figure supplement 2B).

Discussion

We have presented a structural ensemble of the RNF169(UDM2)-H2AK13Cub-NCP complex based on replica-averaged MD simulations that included CSPs and mutagenesis data as experimental restraints. This structural ensemble illustrates how RNF169 is able to discriminate between numerous ubiquitylated chromatin species to specifically bind nucleosomes monoubiquitylated at H2AK13/K15. The multicomponent complex includes a three-pronged interaction involving a MIU2-ubiquitin component and a pair of electrostatic contacts between key arginine residues within the LRM2 module of RNF169 and the acidic patch region of the nucleosome surface. Our model reveals that the MIU2 helix interacts with ubiquitin via a hydrophobic surface centered about A673 of RNF169(UDM2) that involves the canonical binding interface on ubiquitin,

comprised of I44, L8 and V70, similar to a previously published MIU-ubiquitin crystal structure (24). Notably, the LRM2 module remains highly disordered in the complex, with electrostatic contacts between R689 and one or more of H2A E60/E63 and H2B D48, and between R700 and H2A E63, D89 and E91 observed in all members of the calculated structural ensemble. The good agreement between the position of ubiquitin within the structural ensemble and in the cryo-EM map of RNF169-bound ubNCPs provides cross-validation for the position of ubiquitin in the multicomponent complex. Moreover, the cryo-EM data establishes that within the complex ubiquitin is held more rigidly to the nucleosome core, through the combined action of the MIU2 and LRM2, in agreement with NMR based spin relaxation measurements. Finally, because the critical C-terminal MIU2-LRM2 module of RNF169, that confers specificity, is conserved in RNF168 the proposed model for the RNF169(UDM2)-H2AK13Cub-NCP complex is likely a good proxy for the interaction of K13ub-NCPs with RNF168.

The size of the RNF169(UDM2)-ubNCP complex and the intrinsic dynamics of both the histone H2A tail and the LRM2 module pose significant challenges for traditional structural biology techniques which often assume that the experimental restraints define a single conformer. The integrative approach taken here, including the use of methyl-TROSY NMR, mutagenesis, replica-averaged MD simulations and cryo-EM was essential in defining the molecular details of the complex. NMR has evolved in recent years to become a powerful tool for the study of the structure, and in particular the dynamics, of large proteins

512 and protein complexes through the development of optimized protein labeling
513 methods (51-54) and TROSY-based experimental approaches that enhance both
514 spectral resolution and sensitivity (33, 55). Despite the prevalence of methyl
515 bearing residues within protein cores and at interfaces in complexes (56), their
516 scarcity on exposed protein surfaces and within highly charged regions can be
517 limiting in the study of electrostatically driven interactions. Pertinent to this case
518 is the lack of ILV residues on the surface of the NCP. While some well-
519 positioned methyl probes, including V45 and L103 of H2B, were instrumental in
520 identifying the acidic patch as the binding partner for the critical arginine regions
521 of the LRM2, methyl-based NMR strategies alone were insufficient to ascertain
522 the structural details of this complex. Distance restraints are key elements in the
523 elucidation of detailed structures, with short (~5 Å) to long-range (< ~30 Å)
524 distances available from NOE and paramagnetic relaxation enhancement (PRE)
525 NMR techniques, respectively (57, 58). However, the dynamic nature of
526 disordered protein segments can challenge the measurement of intermolecular
527 distances (59). In our hands, intermolecular methyl NOEs between
528 RNF169(UDM2) and NCP histones were difficult to observe, reflecting both the
529 dilute samples used (100 μM) and the paucity of methyl groups at the binding
530 interface. Furthermore, in dynamic systems, such as the one studied here,
531 intermolecular PREs provide at best upper distance bounds that we have found
532 to be too large to be useful for straightforward protein-protein docking
533 approaches. To circumvent these difficulties replica-averaged MD simulations
534 were used to account for the inherent flexibility of both the ubiquitin attachment

and the LRM2 module so as to produce a structural ensemble consistent with our experimental data. Improvements in both the accuracy of the force fields that describe molecular interactions and the available computational power have increased the robustness of MD simulations and the complexity of the systems amenable to them (60, 61). The inclusion of experimental NMR data in MD simulations, as ensemble-averaged restraints, provides a means to more extensively sample the conformational space of interest and to generate ensembles of structures consistent with experimental measurements (62-64). The complementarity of the techniques used here and the continuous effort toward improving their capabilities will facilitate future studies of dynamic macromolecules, similar to the RNF169-ubNCP complex described here.

The present study reveals the molecular details of the interaction between a new class of ubiquitin reader and ubiquitylated NCPs. Recently the cryo-EM derived structure of a complex of a ubiquitylated histone reader, 53BP1, and H2AK15 ubiquitylated-NCP was reported, revealing the basis for a separate class of interaction (13). In the case of 53BP1, this interaction is established via the involvement of a pair of arginine residues flanking the ubiquitin conjugation position in the H2A N-terminal tail, R11 and R17, that straddle the DNA to optimally position ubiquitin for contact with the ubiquitylation dependent recruitment motif (UDR) of 53BP1 (13). Modeling of the UDR region also revealed contact with the acidic patch via a single arginine residue (R1627) (13). The acidic patch surface is a critical component of all chromatin factors bound to the NCP (36-40, 65), where, at a minimum, one anchoring arginine binds a cavity

generated by H2A E60, D89 and E91 side chains. In the case of RNF169, R700 acts as the anchoring arginine, with R689 making contacts of approximately equal importance to the overall stability of the complex. While the topology of the acidic patch can accommodate interactions with a variety of structural types, RNF169, similar to HMGN2 and CENP-C (34, 65), lacks defined secondary structure when bound to the NCP surface.

Ubiquitylation of H2A on K13 and K15 by RNF168 is necessary for the recruitment of downstream repair factors such as RNF169, 53BP1 and BRCA1 (2). The ability of RNF168 to specifically bind its own mark provides both a mechanism for facilitating the amplification of these marks as well as spatial and temporal control over its catalytic activity, ensuring the correct, stepwise execution of the DSB response. Notwithstanding the similarities of the UDM2 domains of RNF168 and RNF169, the affinity of RNF169 for K13 or K15 ubNCPs is higher (Figure 1-figure supplement 1). This may provide an additional level of control on the catalytic activity of RNF168 since as RNF169 accumulates at DSBs, in an RNF168-dependant manner, it can outcompete RNF168 for H2AK13/K15 ubiquitylated NCPs to maintain the ubiquitin signal within a defined region of chromatin surrounding DSBs. A complete understanding of the interplay between the RNF168/169 ubiquitin readers and downstream repair factors 53BP1 and BRCA1, and related implications for the cellular response to DNA damage, are important outstanding questions. In this report, we have presented an ensemble of RNF169(UDM2)-H2AK13Cub-NCP structures illustrating the inherent dynamics of the complex, while revealing the residue-specific contacts

that impart selectivity. Our model shows how relatively weak interactions work synergistically to enable the selection of a specific type of ub-NCP among the diverse array of ubiquitylated chromatin sites in the nucleus.

Materials and Methods

Protein Expression and Purification

For Pull-downs and Cell assays

All MBP and GFP fusion proteins as well as human and xenopus laevis histone genes were prepared as previously described (5, 12). Pull-down experiments (Figures 1C, 1D, Figure 1-figure supplement 1 and Figure 3-figure supplement 1C) made use of various MBP fusion proteins including MBP-RNF168(110-201; DDp2222), MBP-RNF168(374-571; DDp2220), MBP-RNF169(662-708; DDp1675), MBP-RAP80(60-124; DDp1708), and MBP-RAD18(201-240; DDp1698). Human histones genes used to prepare NCPs included pET15b His-H2A (DDp1872), pET15b His-H2B (DDp1873), and from Xenopus laevix pET3d H3 (DDp1874) and pET3a H4 (DDp1875). E2 and E3 enzyme constructs used for catalytic ubiquitylation (Figures 1C, 1D, Figure 1-figure supplement 1 and Figure 3-figure supplement 1C) included pPROEX GST-RNF168 residues 1-113 (DDp1878), His6-UBCH5a (DDp1543), pET24b BMI1-His6 residues 1–108 (DDp1886) and pGEX-6P-1 RING1b residues 1–116 (DDp1887). The GFP-RNF169 used for transfection in cell assays included residues 662-708 (DDp1674) (Figure 5-figure supplement 1).

603 GST and MBP fusion proteins were produced as previously described (5,
604 12, 66). Briefly, MBP and GST proteins expressed in *Escherichia coli* were
605 purified on amylose (New England Biolabs) or glutathione sepharose 4B (GE
606 Healthcare) resins according to the batch method described by the manufacturer
607 and stored in 50mM HEPES pH 7.5, 150mM NaCl, 5% glycerol or in PBS. All
608 protein concentrations were determined via the Pierce BCA assay kit
609 (ThermoFisher), followed by SDS-PAGE Coomassie staining with comparison to
610 known control proteins.

611

612 *For NMR and cryo-EM studies*

613 *D. melanogaster* histone genes for H2A, H2B, H3 and H4 were cloned into a
614 pET21b expression vector, as described previously (67). The *h. sapiens*
615 ubiquitin gene was cloned into a pET28b expression vector which included a
616 thrombin cleavage site replaced with a N-terminal His6-tag and a tobacco etch
617 virus (TEV) cleavage site between the His_6-tag and the protein sequence. The *h.*
618 *sapiens* RNF169(UDM2) gene, encompassing residues 662-708, was cloned into
619 a pET29b+ expression vector that included an N-terminal His_6-SUMO fusion
620 protein removable using SUMO protease Ulp1 (68). RNF169(UDM2) including
621 the DAAA N-terminal helix extension (that increases temperature stability) was
622 purchased from GenScript and sub-cloned into pET29b+. It will be explicitly
623 assumed below that RNF169(UDM2) includes the DAAA extension. All mutants
624 including, H3(C110S), Ub(G76C), H2A(K13C), H2A(E60A/E63A),
625 H2A(D89A/E91A), RNF169(R689A), RNF169(Y697A), RNF169(L699I),

RNF169(R700A), RNF169(S701A), RNF169(R689A/R690A/K691A) and RNF169(L699A/R700A/S701A), were prepared with PfuTurbo DNA polymerase using the QuikChange site-directed mutagenesis method (Strategene). Protein expression was achieved by growing *Escherichia coli* cells at 37°C, transformed with the desired expression plasmid, in media containing 100 mg/L ampicillin for all histones and 50 mg/L kanamycin for ubiquitin and RNF169(UDM2). Expression was induced with 1mM IPTG for 16 hours at 37°C for H2A, H2B and H3, 4 hours at 37°C for H4, 16 hours at 30°C for ubiquitin and 16 hours at 18°C for RNF169(UDM2). Cells were subsequently harvested by centrifugation and purified immediately or stored at -80°C. Unlabeled proteins were expressed in LB media. Protonated, uniformly ^{13}C, ^{15}N-labeled RNF169(UDM2) was grown in 100% H_2O minimal M9 media supplemented with 3 g/L [^{1}H-^{13}C]-glucose and 1 g/L ^{15}N-NH_4Cl. Deuterated histones, ubiquitin and RNF169(UDM2) were expressed in 99.9% D_2O minimal M9 media supplemented with 3 g/L [^{2}H-^{12}C]-glucose. For the expression of ubiquitin, H2A, H2B and H3C110S with Ile-δ1-[$^{13}CH_3$] and Leu/Val-[$^{13}CH_3$,$^{12}CD_3$] methyl labeling (ILV-methyl labeling) (53), 99.9% D_2O minimal M9 media was supplemented with 3 g/L [^{2}H-^{12}C]-glucose, 85 mg/L α-ketoisovaleric acid (L/V labeling) and 45 mg/L α-ketobutyric acid (Ile-labeling) 1 hour prior to induction. All histones were purified from inclusion bodies using HighTrap SP-XL ion exchange columns (GE Healthcare) equilibrated in 7 M urea, 150 mM NaCl, 50 mM Tris pH 8 and eluted using a linear gradient up to 1M NaCl over 9 column volumes. Fractions containing the histone proteins were then pooled, concentrated and further purified using a HighLoad 10/300 S75

superdex gel filtration column (GE Healthcare), followed by extensive dialysis into water and lyophilization. Ubiquitin and RNF169 were purified using Talon metal affinity resin (Clontech), followed by TEV cleavage to remove the His_6-tag (ubiquitin) or Ulp1 cleavage to remove SUMO (RNF169) and a final gel filtration run using a HighLoad 10/300 S75 superdex column equilibrated in 150 mM NaCl, 20 mM Tris pH 7.5 (ubiquitin) or 150 mM NaCl, 20mM sodium phosphate pH 6 (RNF169). Protein purity was evaluated using SDS-PAGE and electrospray ionization-mass spectrometry (ESI-MS).

Peptides

LANA1-23 peptide, (Biotin-LC-MAPPGMRLRSGRSTGAPLTRGSY) and the non-binding LANA1-23 LRS mutant peptide, (Biotin-LC-MAPPGMRAAAGRSTGAPLTRGSY) (Figure 1-figure supplement 1) were synthesized by BioBasic.

DNA preparation

153-bp 601 DNA (69) was prepared from a 32-copy plasmid (a gift from Dr. Tom Muir's lab), transformed into DH5α *Escherichia coli* cells and grown overnight in LB/ampicillin media at 37°C. Following harvest by centrifugation, Giga prep plasmid purification kits (Qiagen, cat.12191) were used to purify the 32-copy plasmid. Digestion using EcoRV (0.5units/μg plasmid) in NEB buffer3 was carried out for 20 hours at 37°C. The resulting solution of liberated 153 bp fragments was treated with 0.3375 volume equivalents of fresh 40% PEG-600 and 0.15 volume equivalents of 5 M NaCl solution and incubated at 4°C for 1

671 hour to precipitate the vector backbone. Following centrifugation at 14,000 rpm
672 for 30 minutes at 4°C, 2.5 volume equivalents of 100% ethanol was added to the
673 supernatant and left at -20°C overnight to precipitate the 153 bp 601 DNA
674 fragments. Following centrifugation at 14,000 rpm for 30 minutes at 4°C, the
675 precipitated DNA pellet was washed once with cold 70% ethanol and
676 resuspended in 10 mM Tris pH 8. The 153 bp 601 DNA fragments were further
677 purified using a HiTrap DEAE-FF column (GE Healthcare) equilibrated in 10 mM
678 Tris pH 8 and eluted using a linear gradient up to 1M KCl over 9 column
679 volumes. Fractions containing DNA were pooled, concentrated and the
680 concentration of KCl was adjusted to 2M for subsequent NCP reconstitution.

681 **Disulfide-directed ubiquitylation of H2A**

682 Purified ubiquitin was prepared for conjugation by the addition of fresh 1,4-
683 dithiothreitol (DTT) at 5 mM concentration to ensure all intermolecular disulfide
684 bonds were reduced. Subsequent removal of DTT was achieved using PD-10
685 desalting cartridges (GE Healthcare). The eluate was flash frozen with liquid
686 nitrogen and subsequently lyophilized. Lyophilized H2AK13C (~5 mg) was
687 resuspended in 1 mL water with 5 mM tris(2-carboxyethyl)phosphine (TCEP) and
688 subsequently activated by the addition of 10-fold molar excess of 2,2'-dithiobis(5-
689 nitropyridine) (DTNP) dissolved in 2 mL of acetic acid. The reaction was allowed
690 to proceed overnight at room temperature and verified by ESI-MS. The activated
691 product (H2A K13C-DTNP) was dialyzed extensively into water to remove
692 unused DTNP, followed by gel filtration using a HighLoad 10/300 superdex S75
693 gel filtration column (GE Healthcare) equilibrated with 6 M guanidine

hydrochloride, 150 mM NaCl, 50 mM TRIS pH 6.9. Following degassing of the H2A K13C-DTNP solution lyophilized UbG76C was added at a 2:1 molar excess to the histone solution and gently agitated for 1 hour to allow for the completion of the reaction. The final product was verified with ESI-MS. The procedure is outlined schematically in Figure 3-figure supplement 1A.

Octamer refolding and NCP reconstitution

Purified H2B, H3C110S, H4 and H2A K13C-Ub were combined at equimolar ratios and refolded into octamers, that were subsequently purified and reconstituted into NCPs as previously described (25) with the exception that β-mercaptoethanol was not added to any buffers. Microscale test NCP reconstitution reactions (50 μL, 7 μM DNA) were used to determine the optimal stoichiometry of Ub-octamers and DNA. The quality and purity of the resulting NCPs were checked using 5% native PAGE and ESI-MS.

Catalytic ubiquitylation of NCPs

Nucleosomes were ubiquitinated by incubating 2.5 μg recombinant mononucleosomes with 30 nM E1 (Uba1), 1.4 mM UBCH5a, 4 mM RNF168 (1–113) (Figures 1C, 1D, Figure 1-figure supplement 1, Figure 3-figure supplement 1C) or BMI1–RING1B complex (Figure 1D), 11 mM ubiquitin (Boston Biochem) and 4 mM ATP in a buffer containing 50 mM Tris-HCl, pH7.5, 100 mM NaCl, 10 mM $MgCl_2$, 1 mM ZnOAc and 1 mM DTT at 30^{o}C for 2 h.

Antibodies

716 For Western blotting shown in Figures 1C, 1D, Figure 1-figure supplement 1 and
717 Figure 3-figure supplement 1C we used the following primary antibodies: rabbit
718 anti-H3 (Ab1791, Abcam – RRID:AB_302613), mouse anti-MBP (E8032, NEB –
719 RRID:AB_1559732), rabbit anti-H2A (raised against amino acid residues 100-
720 130)(12) , and rabbit anti-H2A (targeting 719 the acidic patch, 07-146, Millipore –
721 RIDD:AB_310394). Peroxidase-affiniPure goat anti-rabbit IgG (111 035 144,
722 Jackson Immuno Research – RRID:AB_2307391) and HRP-linked sheep anti-
723 mouse IgG (NA931, GE Healthcare – RIDD:AB_772210) were used as
724 secondary antibodies. For immunofluorescence and FACS analyses, as shown in
725 Figure 5-figure supplement 2, cells were stained for mouse anti-γ-H2AX (clone
726 JBW301, Millipore– RIDD:AB_309864) and rabbit anti-53-BP1 (sc-22760, Santa
727 Cruz – RIDD:AB_2256326). The following antibodies were used as secondary
728 antibodies in immunofluorescence microscopy: Alexa Fluor 555 anti-rabbit and
729 AlexaFluor 647 goat anti-mouse (Molecular Probes – RIDD:AB_141784 and
730 RIDD:AB_141725, respectively). DNA was counterstained with DAPI to trace the
731 outline of nuclei.
732
733 **Cell culture and plasmid transfection**
734 Human cell culture media were supplemented with 10% fetal bovine serum (FBS)
735 and maintained at 37°C and at a 5% CO_2 atmosphere. U-2-OS (U2OS,
736 RRID:CVCL_0042) WT were purchased from ATCC and cultured in McCoy's
737 medium (Gibco). The cell line was tested to be negative for mycoplasma
738 contamination and authenticated by STR DNA profiling. Plasmid transfections

were carried out using Lipofectamine 2000 Transfection Reagent (Invitrogen) (Figure 5-figure supplement 1).

Immunofluorescence microscopy

Cells were grown on coverslips, irradiated with 2Gy and fixed with 2% (w/v) paraformaldehyde in PBS 1h post-irradiation. Cells were then processed for immunostaining as described previously (5, 70, 71). Confocal images were taken using a Zeiss LSM780 laser-scanning microscope and a Leica SP5-II confocal microscope in standard scanning mode. (Figure 5-figure supplement 1)

NCP pull-down assays

NCP pull-downs (Figure 1C, 1D, Figure 1-figure supplement 1 and Figure 3-figure supplement 1C) were performed in a total volume of 100 µL by using 15–20 µL ubiquitination reaction (see **Catalytic ubiquitylation of NCPs** above), 2, 4 or 8 µg MBP-protein coupled to amylose resin (New England Biolabs), in pull-down buffer (50 mM Tris-Cl pH 7.5, 150 mM NaCl, 1 mM DTT, 0.05% NP-40, 0.1% BSA). Pull-down reactions were incubated for 2 h at 4°C. Pull-downs were then washed three times with 0.75 mL of the pull-down buffer plus 0.1% BSA and eluted in Laemmli SDS–PAGE sample buffer for analysis by immunoblotting. Pull-downs presented in Figure 3-figure supplement 2B were eluted in Laemmli SDS–PAGE without DTT to preserve the integrity of chemically labeled ubK13C- or ubK15C-H2A NCPs. For the competition assay (Figure 1-figure supplement 1) the pull-down was performed as normal, with the addition of LANA peptide, MBP-

762 RNF168(UDM2) or MBP-RNF169(UDM2) during the incubation with ubiquitylated
763 NCP.
764
765 **Circular dichroism spectroscopy**
766 Circular Dichroism (CD) spectra and temperature melts of RNF169(UDM2)
767 without and with the DAAA N-terminal helix extension (Figure 2-figure
768 supplement 1B) were acquired using a Jasco J-815 CD Spectrometer (Jasco,
769 Inc.) and a 0.1 cm path length cuvette. CD spectra were collected as an average
770 of 3 scans between 190 and 240 nm using a 20 nm/min scanning rate, 8 s
771 response time and protein concentrations in the range of 50-65 μM. For
772 temperature melts elipticity at 222 nm was monitored over a temperature range
773 of 10 to 70°C with a temperature slope of 1°C/min and protein concentrations
774 were in the 25-35 μM range. Raw data was corrected for buffer contributions and
775 converted to percent helicity as previously described (72, 73).
776
777 **NMR experiments**

778 All NMR experiments on NCPs were performed at 45°C using 14.0 T Varian
779 Inova or Bruker Avance III HD spectrometers equipped with cryogenically cooled
780 pulse-field gradient triple-resonance probes. The assignment of RNF169(UDM2)
781 and titrations of free ubiquitin with RNF169(UDM2) were performed at 35°C and
782 45°C, respectively, on a 11.7 T Varian Inova spectrometer with a room
783 temperature pulse-field gradient triple-resonance probe. The NMR buffer for H2A
784 K13Cub-NCP samples contained 100 mM NaCl, 0.05% azide, 0.5%

785 trifluoroethanol and 20 mM sodium phosphate pH 6, 99.9% D_2O, with sample
786 concentrations in the range of 50-100uM in NCP, as determined by A260
787 measurement of DNA. The NMR buffer used for the assignment of
788 RNF169(UDM2) contained 100 mM NaCl, 0.05% azide, and 20 mM sodium
789 phosphate pH 6, 90% H_2O/10% D_2O with 0.62 mM protein concentration. All
790 NMR data were processed and analyzed using the suite of programs provided in
791 NMRPipe/NMRDraw and NMRviewJ software packages (74, 75), with backbone
792 assignments carried out using CCPnmr (76).

793 Translational diffusion coefficients (Figure 3-figure supplement 1B) were
794 measured by recoding a series of 1D ^{13}C-edited spectra at 25°C using a pulse
795 sequence analogous to an ^{15}N-edited experiment published previously (26), with
796 the ^{15}N pulses exchanged for ^{13}C pulses. After initial gradient encoding of the
797 magnetization a constant-delay diffusion element of 150 ms for free ubiquitin (8.9
798 kDa) or 200 ms for ¼ proteasome (180 kDa) and H2AK13Cub-NCP (235 kDa)
799 was employed. The resulting ^{1}H methyl signal was integrated to quantify
800 intensities as a function of gradient strength. Diffusion constants were obtained
801 by nonlinear least square fits of peak intensities as a function of the square of the
802 gradient strength to the relation $I = I_o\exp(-aDG^2)$ where I and I_o are the integrated
803 peak intensities in the presence and absence of the gradient G, respectively, D is
804 the diffusion constant and a is a constant comprised of experimental parameters.

805 Backbone resonance assignments of RNF169(UDM2) (Figure 2) were
806 completed using 2D ^{1}H-^{15}N HSQC and 3D HNCACB, HNCACO, HNCO and
807 CBCA(CO)NH experiments (20, 77, 78), with side-chain assignments obtained

using 3D H(C)(CO)NH-TOCSY and (H)C(CO)NH-TOCSY experiments (79, 80). Stereospecific assignments of leucine and valine residues were achieved as previously described (81). Briefly, RNF169(UDM2) was prepared in 100% H_2O M9 minimal media supplemented with 10% [^{1}H,^{13}C]-glucose/90% [^{1}H,^{12}C]-glucose; subsequent analysis of CT-HSQC spectra (82, 83) produced assignments of leucine $\delta1/\delta2$ and valine $\gamma1/\gamma2$ resonances.

^{1}H-^{13}C HMQC spectra of nucleosomes were recorded exploiting a methyl-TROSY effect to obtain high quality spectra (33, 84). Assignments of all ILV methyl resonances within the histones and ubiquitin were transferred from those previously published (67, 84). Chemical shift perturbations were measured using ^{1}H-^{13}C HMQC spectra of free H2AK13Cub-NCP and H2AK13Cub-NCP saturated with 2.5-fold excess RNF169(UDM2). Weighted CSPs of ILV residues were calculated according to:

$$CSP = \sqrt{\Delta\delta_{H,i}^2 + \Delta\delta_{C,i}^2 \cdot w_i} \quad (1)$$

where $\Delta\delta_i$ is the difference in chemical shift between the free and bound states (ppm) for a given isoleucine, leucine or valine resonance i, and the chemical shift weighting factor w_i was set to $\frac{\sigma_{H,i}}{\sigma_{C,i}}$ (~0.16-0.18), where σ_i is the standard deviation of deposited chemical shifts for isoleucine, leucine and valine methyl resonances in the Biological Magnetic Resonance Data Bank (BMRB, http://www.bmrb.wisc.edu) for atom i (67).

Titrations (Figures 3A, 3B and Figure 3-figure supplement 2) were carried

out by increasing the ratios of [RNF169]/[Ub] ([RNF169]/[H2AK13Cub-NCP]) from 0 to 42 in a series of 10 ^{1}H-^{13}C CT-HSQC experiments (from 0 to 2.6 over a series of 16 ^{1}H-^{13}C HMQC data sets). The titrations were followed via ^{13}C Ub that was either uniformly labeled (titration of Ub) or ILV-methyl labeled (titration of K13Cub-NCP). For the titration of ^{13}C-labeled RNF169(UDM2) (Figure 3-figure supplement 3) the ratio of [ub]/[RNF169] was increased from 0 to 6 in a series of ^{1}H-^{13}C CT-HSQC experiments at 35°C. Note that there are two equivalents of Ub for each NCP and we have assumed independent binding of RNF169 to each Ub site. K_D values were extracted from nonlinear least square fits of the resulting binding isotherms that were obtained by extracting chemical shifts in either ^{13}C or ^{1}H dimensions of ^{1}H-^{13}C correlation plots via:

$$\Delta\delta' = \Delta\delta'_{MAX} \frac{[L]_T + [P]_T + K_d - \sqrt{([L]_T + [P]_T + K_d)^2 - 4[P]_T[L]_T}}{2[P]_T} \quad (2)$$

where $[P]_T$ and $[L]_T$ are the total concentration of Ub and RNF169, respectively, $\Delta\delta'$ is the chemical shift change (relative to the RNF169-free spectrum) at each titration point, and $\Delta\delta'_{MAX}$ is the difference between free and bound chemical shifts. Positions of individual peaks in fast exchange on the NMR chemical shift timescale were fit and reported errors in K_D correspond to one standard deviation of these values.

Kinetic parameters for the RNF169 + H2AK13Cub-NCP binding reaction (Figure 3C) were obtained via line-shape analysis using a K_D value of 24±7μM obtained from chemical shift titration data. Experimental line-shapes (^{13}C dimension) were extracted for I44δ1 of ubiquitin for a range of

851 [RNF169]/[H2AK13Cub-NCP] values and fit using scripts written in MATLAB
852 (MathWorks Inc.), as previously described (30). Intrinsic transverse relaxation
853 rates were estimated from linewidths in ^{1}H-^{13}C HMQC spectra and were not used
854 as fitting parameters. Peak intensities for each titration point (each
855 [RNF169]/[H2AK13Cub-NCP] ratio) were scaled to account for differential line
856 broadening in the ^{1}H dimension that can affect intensities of extracted ^{13}C traces.
857 Fitted parameters included k_{on} and an adjustable coefficient for each titration
858 point, as described above.

859 ILV-methyl group dynamics (Figure 7D) have been measured for ubiquitin
860 in H2AK13Cub-NCP whereby the build-up of methyl ^{1}H triple quantum coherence
861 is quantified as described previously (48). Data sets were recorded in the
862 presence and absence of RNF169(UDM2), 45°C. Relaxation delay values of 1, 2,
863 3, 4, 5, 6, 7, 8, 9, 10, 12 and 14 ms were used and peak intensities
864 corresponding to the build-up of triple quantum coherences (I_a) and the evolution
865 of single quantum coherences (I_b) quantified from 2D spectra at each relaxation
866 delay. Values of the product of the square of the methyl axis order parameter, S^2,
867 and the tumbling time of the complex, τ_C, ($S^2\tau_C$) were extracted from nonlinear
868 least square fits of build up curves of I_a/I_b as a function of relaxation delay (48).

869 Distances connecting ubiquitin and RNF-169 in an RNF169(UDM2) –
870 ubiquitin complex were obtained by recording a ^{1}H-^{1}H NOESY data set (mixing
871 time of 200 ms, 20^{o}C) as a first step in generating the structure of the
872 RNF169(UDM2) - H2AK13Cub-NCP complex (Figure 6B). The sample was ILV-
873 methyl labeled in ubiquitin and uniformly ^{13}C labeled in RNF169(UDM2) and was

prepared using an approximate 8-fold excess of RNF169 over ubiquitin. NOEs between A673 of RNF169 and ubiquitin are particularly important as A673 has been shown to be a central player in the interaction in a crystal structure of the Rabex MIU-ub complex (24).

Electron cryo-microscopy

Holey EM grids were prepared by nanofabrication with arrays of 500-800 nm holes as described (85), with the alteration of Gold evaporation onto the grids as a specimen support, rather than carbon (86). For initial screening H2AK13Cub-NCP and RNF169(UDM2) were incubated at a 1:2.5 molar ratio in 10 mM Tris-Cl pH 7.5, 200 mM KCl, 1 mM EDTA and differentially PEG precipitated as described (13); the sample was diluted to 50 mM KCl immediately prior to grid preparation. The low-salt complexes were applied to grids and allowed to equilibrate for 5 s in a FEI Vitrobot and blotted for 10 s prior to freezing in a liquid ethane/propane mixture (1:1 v/v). Grids were stored in liquid nitrogen, prior to transfer to a Gatan 626 cryotransfer specimen holder. Samples were imaged with a FEI F20 electron microscope, equipped with a field emission gun and operating at 200 kV. Movies were acquired manually in counting mode with a Gatan K2 Summit direct detector device camera using a calibrated magnification of 34,483×, resulting in a physical pixel size corresponding to 1.45 Å. During movie acquisition the sample was exposed to 1.2 electrons/$Å^2$/frame and a total exposure of 36 electrons/$Å^2$ on the specimen.

Image acquisition and data analysis revealed that only a subset of RNF169(UDM2) was bound to H2AK13Cub-NCP under the preliminary

screening conditions. 175 movies were acquired for this preliminary dataset. The formation of RNF169(UDM2)-ubNCP complexes was optimized by incubating a 1:5 molar ratio of H2AK13Cub-NCP to RNF169(UDM2) in 10 mM tris pH 6.8, 30 mM KCl and 1mM EDTA followed by differential PEG precipitation as described (13), with the exception that a higher final PEG-4000 concentration of 9% (v/v) was used. A total of 867 movies were acquired for this sample consisting of RNF169(UDM2)-bound ubNCPs.

Individual frames in a movie stack were aligned and averaged using the programs alignframes_lmbfgs and shiftframes (87). The contrast transfer function (CTF) was calculated from the averaged frames using CTFFIND4 (88). Manual inspection of micrographs and their corresponding power spectra was performed in Relion 1.3 (89). Poor micrographs with ice contamination were discarded. Particle selection, based on manually selected templates, was performed in Relion 1.3. A total of 42,343 and 301,275 particle images were selected for the ubNCP and RNF169(UDM2)-ubNCP maps, respectively. After particle image extraction, beam induced particle motion between frames was corrected with alignparts_lmbfgs (87). A previously measured magnification anisotropy from the Toronto F20 electron microscope was corrected (90). Extracted particle images were subject to 2D classification in Relion 1.3 and high-resolution class averages were selected for 3D classification (Figure 7-figure supplement 1B). A low pass filtered model of NCP based on PDB: 1KX5 (91) was used as an initial template for 3D classification. For the preliminary dataset of free ubNCP, 3D classification was performed using 4 classes. One class, populated with 60% of the total

920 particles (11,063 particles) was refined further to yield the 8.1 □ H2AK13Cub-
921 NCP structure (Figure 7A, 7C). For the dataset of RNF169(UDM2)-bound NCPs
922 3D classification was performed with 5 classes. Particle images from one class
923 populated with 35% of the total particles (31,760 particles) showed high-
924 resolution features and was refined further (Figure 7-figure supplement 1C). The
925 RNF169(UDM2)-ubNCP refined map was sharpened in Relion 1.3 with a B-factor
926 of -200. Global resolution estimates were determined using the FSC=0.143
927 criterion after a gold-standard refinement (Figure 7-figure supplement 1D and 1E)
928 (92). Local resolution was estimated with ResMap (47). Calculations with Relion
929 1.3 were performed using the Hospital for Sick Children high performance
930 computing facility.
931
932 **Haddock Docking**

933 An atomic resolution model of the MIU2-ubiquitin complex (extending from K662
934 to N682 of RNF169, see Fig. 2A) was generated by using the HADDOCK
935 modeling program (Figure 6C) (42). The structure of (isolated) ubiquitin that was
936 used in the docking procedure was taken from an X-ray model of a complex of
937 the Rabex MIU with ubiquitin (PDB 2C7M, chain B) (24). The structure of the
938 MIU2 motif for the HADDOCK calculations was built as a homology model based
939 on the Rabex MIU, corresponding to chain A of PDB 2C7M using the program
940 MODELLER (93). Since the C-terminal LRM region of RNF169 is largely
941 disordered (see below) only the N-terminal MIU2 element was included at this
942 stage. In order to carry out the docking study, a list of ‘active’ and ‘passive’

residues was defined as required by HADDOCK. Residues L672, A673, L676 of RNF169 and residues L8, I44, V70 of ubiquitin were defined as ‘active’ residues based on NMR titration results (Figures 6A, Figure 3A, Figure 3-figure supplement 3) and solvent accessibility criteria, while ‘passive’ residues were calculated using the standard procedure in HADDOCK. It is worth noting that NMR titration data indicate that several additional ubiquitin residues (I30, I36, I61, L67) have CSPs upon titration with MIU2 and these could potentially be involved in binding as well. They were not included as ‘active’ residues, however, since the methyl groups of these Ile/Leu probes were buried inside the hydrophobic core, with low solvent accessibilities. We employed a minimum of 20% relative solvent accessibility as a cut off for inclusion as an ‘active’ residue. This is reduced from the recommended value of 40% used for backbone atoms in Haddock calculations, as methyl groups are less exposed. Additional restraints, measured from a 200 ms mixing time NOE spectrum of an RNF169(UDM2) – ubiquitin complex, were used. These were added in a qualitative manner as upper bound distances of 7 Å between methyl protons of A673 (RNF169) and I44δ1, L8δ1, L8δ2 (ubiquitin). Docking was performed using a standard HADDOCK protocol, and the number of structures selected after the *it0*, *it1* and *itw* stages were 1000, 200, 200 respectively. The final 200 structures were subject to cluster-analysis. Notably, the largest cluster has the lowest average energy and the lowest HADDOCK score in this cluster (also lowest score of all final structures in any cluster) reproduces the binding interface in the X-ray structure of the Rabex MIU-ubiquitin complex (PDB 2C7M), with the key

feature that A673 of MIU2 is located within the hydrophobic binding pocket formed by L8, I44 and V70 of ubiquitin. This structure was selected for further MD simulation studies, as described below. A list of synthetic NOE restraints were constructed based on this representative structure and these were imposed during the MD simulations in order to maintain the HADDOCK generated MIU2-ubiquitin complex. The total number of restraints was 331, which included atomic pairs in the MIU2-ubiquitin complex less than 5 Å. It is worth noting that we have repeated the calculations described above by modifying the upper distance to 10 Å between methyl protons of A673 and neighboring protons on ubiquitin. The structures within the lowest energy cluster were the same as those obtained from the original calculation using 7Å.

Molecular Dynamics Simulations

The simulations described here, summarized schematically in Figure 8-figure supplement 1, were performed using the Parmbsc1 (94) and Amberff99SB* (95) force fields for modeling the DNA and the protein component of the RNF169(UMD2) - H2AK13ub-NCP complex, respectively, along with the TIP3P water model (96). All simulations were carried out using the software package GROMACS (97) modified with PLUMED2, an open source library for free energy calculations (98) and Almost (99), a plugin for NMR chemical shift restraints. A time step of 2 fs was used together with LINCS constraints (100). The van der Waals interactions were implemented with a cutoff of 1.2 nm and long-range electrostatic effects were treated with the particle mesh Ewald method and a cut-off of 0.9 nm (101).

Starting model

An initial model for the MIU2-ubiquitin complex was created using the docking program Haddock (102), as described above, with the structure of ubiquitin given by PDB ID: 1UBQ (24). Synthetic NOEs that enforced the obtained Haddock structure were used in most of the subsequent computations, as described below and illustrated in Figure 8-figure supplement 1. The MIU2-ubiquitin complex was covalently attached to the NCP 'in silico', via a disulfide bond linkage connecting C76 and C13 of ubiquitin and H2AK13C, respectively, using GROMACS (97). This linkage mimics the chemical ligation of ubiquitin and H2A that has been used experimentally (see text). The C-terminal end of RNF169 (residues 683-708) and the N-terminal end of H2A (residues 1-11) were appended to MIU2 and H2A, respectively, using Modeller (103). In this manner an initial complex was created containing a pair of ubiquitin molecules / NCP, one attached to each H2A. The model was protonated and solvated with 88,385 water molecules and 150 mM NaCl (as in the NMR experiments) in a dodecahedron box of 1,950 nm^3 volume. The system was first energy minimized for 10,000 steps using the steepest descent algorithm, equilibrated in the position restrained NVT ensemble at 300 K for 1 ns, and further equilibrated for 1 ns in the position restrained NPT ensemble using the Berendsen barostat (104). All simulations were carried out in the canonical ensemble by keeping the volume fixed and by thermosetting the system with the modified Berendsen thermostat (105). The disordered part of RNF169, comprising the important LRM2 region, was guided toward the canonical acidic patch of the NCP by applying a restraining potential on a

calculated distance *d*, according to

$$E_{wall} = \begin{cases} k(d - d_{max})^2, d > d_{max} \\ 0 \qquad\qquad\quad , d \leq d_{max} \end{cases} \tag{3}$$

where *k* is an energy constant set to 20 kJ/(mol nm^2), d_{max} is a maximum distance set to 25 Å and *d* is the calculated distance between the centers of mass of two groups of so-called active residues, generated from CSP and mutagenesis experiments as being 'points of interaction' between RNF and the NCP. Active residues from one group belong to RNF169, identified by mutation, and include R689, Y697, L699, R700 and S701. Active residues from a second group belong to the NCP and include L50, L57, E60, E63, L64, D89, E91 (H2A) and V45, L99 and L103 (H2B), established on the basis of CSPs and mutagenesis. After approximately 50 ns the restraining potential E_{wall} dropped to 0 (*i.e.*, the distance between the two centers of mass was less than d_{max}). The simulation was then extended for an additional 25 ns with the same restraining potential (Eq. 3). A set of 331 synthetic NOEs was used to enforce the original HADDOCK structure of the MIU2-ubiquitin complex throughout the full 75 ns of simulation. This was achieved via a potential of the form

$$E^{NOE} = \beta \sum_{i=1}^{noes} \left(d_i^{model} - d_i^{cal}\right)^2 \tag{4}$$

where the summation includes all NOEs in the synthetic set, d_i^{model} and d_i^{cal} are distances from the initial HADDOCK model and calculated from the structure during the simulation, respectively, and the coefficient β is set to 0.25 kJ/(mol nm^2). The extended trajectory was used to select four starting conformers (time

points: 10 ns, 15 ns, 20 ns and 25ns) for a replica-averaged simulation with four replicas (Figure 8-figure supplement 1). Before carrying out the replica-averaged simulation, each of the four structures was equilibrated in the position restrained NVT ensemble at 300 K for 5 ns and in the position restrained NPT ensemble for an additional 5 ns.

***Replica averaging*.** Replica-averaged molecular dynamics simulations (17, 50, 106) were performed using all structural restraints as replica-averaged. These restraints included the chemical shifts measured for MIU2 in the unbound state that were applied to restrain the average value of the CamShift back-calculated NMR chemical shifts of MIU2 (107) using the restraining potential,

$$E^{CS} = \alpha \sum_{\mathrm{k}=1}^{21} \sum_{\mathrm{l}=1}^{5} \left(\delta_{\mathrm{kl}}^{\exp} - \frac{1}{M} \sum_{m=1}^{M} \delta_{\mathrm{klm}}^{\mathrm{calc}} \right)^2 \quad (5)$$

where α is the force constant, k, l and m run over 21 residues that include the MIU2 region (k), all five backbone nuclei for which chemical shifts have been measured (l: C_α, C', H_α, H_N and N) and M = 4 replicas (m), respectively. Also included are the derived NOE distances between MIU2 and ubiquitin, based on the HADDOK model of the MIU2-ubiquitin complex, that were used as replica-averaged structural restraints using the restraining potential

$$E^{NOE} = \beta \sum_{i=1}^{noes} \left(d_i^{model} - \left(\frac{1}{M} \sum_{m=1}^{M} \left(\frac{1}{r_m^6} \right) \right)^{-\frac{1}{6}} \right)^2 \quad (6)$$

where β is the force constant and i and m run over the measured NOE restraints and the M = 4 replicas, respectively. It should be emphasized that the NOE

potential is used to ensure that the structure of the ubiquitin/MIU2 helix, as determined by HADDOCK docking (see above), is preserved during the molecular dynamics calculations. To this end we have used a series of 331 synthetic NOEs based on the HADDOCK model that guide ubiquitin/MIU2 helix docking during molecular dynamics. While the $1/r^6$ term in Eq. 6 does assume that averaging between replicas is slow compared to the overall tumbling of the NCP complex (~100 ns) this level of detail does not affect the resulting ubiquitin/MIU2 structures that are simply enforced to their HADDOCK model by this procedure. CSPs and mutagenesis data were taken into account in the following manner. For each active residue belonging to RNF169 the number of contacts with active residues from the NCP was calculated as

$$S_i = \sum_j s_{ij} \tag{7}$$

where *i* and *j* are active residues belonging to the RNF169 and to the NCP, respectively, s_{ij} is 1 if a contact between any atom of residues *i* and *j* is formed and zero otherwise. The distance for the contact switching function was set to 6.5 Å in a first set of simulations and 10 Å in a second set; the structural features of the resulting ensembles do not change. The number of contacts S_i was enforced to be larger than 1 in at least one replica at each time point of the simulation using a restraining potential of the same type as in Eq. 3. Thus, the experimental measurements were used to modify the underlying force field on the fly by employing a replica averaging procedure whereby back-calculated parameters are compared with their experimentally measured values. In this procedure the system evolves with a force field that is perturbed to increase the agreement with

the experimental restraints.

In the first 75 ns of the replica-averaged simulation the values for the force constants α (Eq 5), β (Eq. 6) and k (for the contact number, Eq. 3) were gradually increased until the restraining potentials reached a plateau. The value of the force constant α was increased over a range extending from 0-24 kJ/(mol ppm^2) in steps of 1 kJ/(mol ppm^2), β was increased in the range 0-2 kJ/(mol nm^2) in steps of 0.1 kJ/(mol nm^2) and k in the range 0-50 kJ/(mol nm^2) in steps of 1 kJ/(mol nm^2). The simulation was then extended for an additional 125 ns. Only the final 50 ns of the extended simulation were used for the analysis of the RNF169(UDM2) H2AK13ub-NCP complex by saving the NCP structure every 1 ps and NCP+water every 10 ps.

***Simulated annealing*.** Although the use of replica-averaged structural restraints enables one to improve the quality of the force field, it requires substantial computational resources to exhaustively sample the conformational space of a system as large as the one studied here. In this regard, we have further verified that R700 is the RNF169 anchoring arginine in our model by performing a series of annealing cycles between 300 K and 500 K using the final conformations of the four replicas (one each) as starting structures. The simulations were performed without the use of the experimental restraints and each annealing cycle lasted for 1 ns. In particular, the system was initially heated from 300 K to 500 K for 400 ps, kept at 500 K for 100 ps, cooled down to 300 K for 400 ps and then finally to 300 K for 100 ps. The total simulation time was 50 ns per replica (50 annealing cycles per replica). Subsequent analysis was performed only on

structures extracted from low constant temperature frames (300 K), by saving conformers at the end of each annealing cycle. It is noteworthy that R700 always remains in the canonical anchoring position in the acidic patch.

To explore the possibility that R689, a second arginine residue that has been shown by mutagenesis to play an important role in the RNF169-NCP complex, can also serve as the 'canonical' anchoring arginine, we carried out combined restrained MD and simulated annealing simulations starting from the final conformation that was produced from one of the four simulations during the replica averaging procedure discussed above. Here the side chain of R689 was forced into the acidic patch of the NCP, lined by E60, D89 and E91 using a restrained MD simulation with a restraining potential of the same type as in Eq. 3. The minimal number of contacts between these 3 acidic patch residues and R689 was set to 10 and the distance for the switching function (d_{max} in Eq. 3) was 6.5 Å. The restrained simulation was carried out by increasing k in the range 0-80 kJ/(mol nm^2), in steps of 4 kJ/(mol nm^2). After approximately 20 ns of simulation time the restraining potential dropped to 0, indicating that R689 occupied the canonical arginine position in the acidic patch of the NCP. The final structure of this restrained simulation was then used as the starting conformer in a simulated annealing procedure identical to the one described above. The annealing was performed without the use of the experimental restraints and with a total simulation time of 30 ns (30 annealing cycles). After the first 8 annealing cycles R689 no longer occupied the canonical position and by approximately 18 ns it was replaced by R700 that remained in the canonical position until the end of the

simulation.

Acknowledgement

This work was supported by grants from the Canadian Institutes of Health Research to L.E.K and D.D. (FDN143343), by a Grant-in-Aid from the Krembil Foundation (D.D.) and by a Scholarship for the Next Generation of Scientists from Cancer Research Society (A.F-T.). J.K-L was supported by a fellowship from the Leukemia and Lymphoma Society. L.E.K., D.D., C.H.A., and A.F-T hold Canada Research Chairs in Biochemistry, in Molecular Mechanisms of Genome Integrity, in Structural Genomics, and in Molecular Virology and Genomic Instability, respectively. The SGC is a registered charity (number 1097737) that receives funds from AbbVie, Bayer Pharma AG, Boehringer Ingelheim, Canada Foundation for Innovation, Eshelman Institute for Innovation, Genome Canada through Ontario Genomics Institute, Innovative Medicines Initiative (EU/EFPIA) [ULTRA-DD grant no. 115766], Janssen, Merck & Co., Novartis Pharma AG, Ontario Ministry of Economic Development and Innovation, Pfizer, São Paulo Research Foundation-FAPESP, Takeda, and the Wellcome Trust.

Competing interests

The authors declare no competing interests.

Figure 1. **RNF168 and RNF169 bind RNF168-ubiquitylated NCPs. A**. Schematic of RNF8 mediated DNA DSB repair pathway. ATM: Ataxia telangiectasia mutated, MDC1: mediator of DNA damage checkpoint 1, BRCT: breast cancer 1 C-terminal, H1: linker histone H1, RNF: ring finger proteins, 53BP1: p53 binding protein 1, Ub: ubiquitin, P: phosphate group, Me: methyl group. **B.** Domain architecture of RNF168(1-571) and RNF169(1-708). Domains and motifs are

indicated. R: RING domain, MIU: motif interacting with ubiquitin, UIM: ubiquitin-interacting motif, UMI: UIM-, MIU-related ubiquitin binding motif, LR: LR motif. **C.** MBP pull-down assays of RNF168-ubiquitylated nucleosome core particles (H2AK13/K15ub-NCP) with the indicated MBP fusion proteins (RNF168-UDM1(110-201), RNF168-UDM2(374-571), RNF169-UDM2(662-708), RAP80(60-124) and RAD18(201-240)). Input: 5% of the amount of ubiquitylated NCPs used in the pull-down. The migration of molecular mass markers (kDa) is indicated on the left. **D.** Pull-down assays of NCPs ubiquitylated with the indicated E3s by either MBP–RNF169(UDM2) (left) or MBP–RNF168(UDM2) (right). A reaction without E3 (-) acts as a negative control. B/R: BMI1/RING1b. **E.** Structure of the nucleosome (PDB: 2PYO (108)). One copy of H2A and H2B is labeled in yellow and in red, respectively. Lysines that are ubiquitylated by RNF168 (H2A K13/K15) and BMI1/RING1B (H2A K118/K119) are indicated in space filling representation.

Figure 2. Solution NMR analysis of RNF169(UDM2) reveals a flexible LRM2. A. Primary sequence of MIU2 (orange) and LRM2 (blue) modules of both RNF169 and RNF168. Conserved residues are indicated with vertical bars. **B.** Assigned ^{1}H-^{15}N HSQC spectrum of ^{15}N,^{13}C-labeled RNF169(UDM2). Data collected at 11.7 T, 35°C. **C.** Output from SSP program (21) using RNF169(UDM2) backbone chemical shifts as input. Corresponding primary sequence of RNF169(662-708) displayed along horizontal axis, with MIU2 (orange) and LRM2 (blue) regions highlighted. Positive and negative SSP values indicate α-helical and β-strand secondary structure propensities, respectively.

Figure 3. Thermodynamics and kinetics of the RNF169(UDM2)-H2AK13C ub-NCP interaction. A. Selected regions of ^{1}H-^{13}C HMQC spectra of ILV-methyl labeled ubiquitin in H2AK13Cub-NCPs with increasing amounts of unlabeled RNF169(UDM2). Arrows indicate direction of peak movement. Data collected at 14.1 T, 45°C. **B.** Chemical shift derived binding curves for selected residues in ILV-methyl labeled ubiquitin in H2AK13Cub-NCPs (left panel) and free ILV-methyl labeled ubiquitin (right panel) upon addition of unlabeled RNF169(UDM2) (circles), with best fits (solid lines) shown. Ratio of RNF169(UDM2) to ubiquitin indicated on horizontal axis. **C.** Fitted line shapes for I44δ1 (extracted from ^{1}H-^{13}C correlation spectra by taking traces along the ^{13}C-dimension). Experimental data in black, with simulated line shapes in red. Ratio of ubiquitin to RNF169(UDM2) indicated in each panel and vertical grey dashed lines denote the resonance positions of I44δ1 in the absence (free) and presence (bound) of saturating amounts of RNF169(UDM2). The extracted kinetic parameters for the RNF169, ub-NCP binding reaction are shown above the traces.

Figure 4. NMR and mutagenesis identify the nucleosome acidic patch as the binding interface for RNF169(UDM2). A. Superimposed ^{1}H-^{13}C HMQC spectra of ILV-methyl labeled H2A (left panel) and ILV-methyl labeled H2B (right panel) in the context of the H2AK13Cub-NCP without (black) and with (yellow, left; red, right) wild-type RNF169(UDM2), respectively. RNF169(UDM2) was added at 2.5-fold excess relative to ubiquitin. Arrows indicate peak movement. Data collected at 14.1 T, 45°C. **B.** Chemical shift perturbations (CSPs) in ILV-methyl labeled H2A (yellow, top panel) and ILV methyl-labeled H2B (red, bottom panel) H2AK13Cub-NCPs. Residues with CSP values 1σ above the average are indicated black line). CSPs were calculated as described in Materials and Methods. **C.** Location of residues with significant CSPs in H2A (yellow) and H2B (red) shown in space filling representation and indicated with arrows on nucleosome crystal structure (2PYO) (46). Acidic patch residues are shown in stick representation and coloured black. H2A: light yellow, H2B: salmon, H3: light blue and H4 :light green. **D.** Selected isoleucine regions of ^{1}H-^{13}C HMQC spectra of free (black) and 2.5-fold excess RNF169(UDM2) bound (red) ILV-methyl labeled ub H2AK13Cub-NCP. Spectra of acidic patch mutant NCPs, H2AK13C(D89A/E91A)ub-NCP (purple, left panel) and H2AK13C(E60A/E63A)ub-NCP (teal, right panel), with 5-fold excess RNF169(UDM2) to ubiquitin are overlaid and highlight the resulting binding deficiency. All data are recorded at 14.1 T, 45°C.

Figure 5. R689 and L699/R700 are critical to the formation of the complex. Isoleucine region of ^{1}H-^{13}C HMQC spectra of ILV-methyl labeled ub H2AK13C-ubNCP without (black) and with (red) wild-type RNF169(UDM2) and the indicted RNF169(UDM2) LRM2 mutants. The ratio of wild-type or mutant RNF169(UDM2) to ubiquitin was 2.5:1 in all cases.

Figure 6. The RNF169 MIU2-ubiquitin interaction involves the canonical binding surface of ubiquitin and a central alanine in the MIU2. A. Overlaid regions of ^{1}H-^{13}C CT-HSQC spectra of ^{13}C-labeled RNF169(UDM2) upon addition of increasing amounts of free ubiquitin. Residues with significant chemical shift changes are labeled. Data recorded at 11.7 T, 35°C. **B.** Selected region of ^{1}H-^{1}H NOESY spectrum of ILV-methyl labeled ubiquitin and ^{13}C-labeled RNF169(UDM2) at 1:8 molar ratio (200 ms mixing time). Cross peaks between A673 of RNF169(UDM2) and I44δ1, L8δ1/δ2 of ubiquitin are indicated. Data recorded at 14.1 T, 20°C. **C.** Signature MIU primary sequence; x: any amino acid type, : large hydrophobic and #: acidic. Structural model of RNF169(MIU2)-ubiquitin from HADDOCK docking calculations, aligned for comparison with crystal structure of the Rabex(MIU)-ubiquitin complex (2C7N (24)). Signature MIU residues within RNF169(MIU2) and Rabex and hydrophobic patch residues are shown in stick representation. Ubiquitin: magenta, RNF169(MIU2): orange, Rabex(MIU): cyan.

Figure 7. Ubiquitin is highly dynamic in the absence of RNF169(UDM2). A. H2AK13Cub-NCP cryo-EM map at 8.1 Å resolution and **B.** RNF169(UDM2) bound H2AK13Cub-NCP cryo-EM map at 6.6 Å resolution including the drosophila NCP crystal structure (2PYO) (46) fit within the map as a rigid body using UCSF chimera. **C.** Indicated equivalent lateral slices through free H2AK13Cub-NCP (left panels) and RNF169(UDM2) bound H2AK13Cub-NCP maps (right panels), showing the raw map density and colored according to local resolution estimates (47). **D.** Histogram comparison of $S^2\tau_C$ values obtained for ILV-methyl labeled ubiquitin in free (blue) and RNF169(UDM2) bound H2AK13Cub-NCPs (pink) fit to a normal distribution.

Figure 8. Structural model of the RNF169(UDM2)-ubNCP complex. A. Alignment of ten representative members of the RNF169(UDM2)-ubNCP structural ensemble obtained from replica-averaged MD simulations constrained by CSPs and mutagenesis data. Histones H2A and H2B were used to align the structures with only one copy of the histones and DNA shown for simplicity. Ubiquitin: magenta, RNF169(662-682)(MIU2): orange, RNF169(683-708)(LRM2): blue, H2A: yellow, H2B: salmon, H3: light blue, H4: light green, DNA: gray. **B.** Enlarged view focusing on specific contacts between R689 and R700 and the nucleosome acidic patch in two separate structures. **C.** Two viewpoints of ten aligned members of the RNF169(UDM2) ub-NCP structural ensemble fit into the RNF169(UDM2) bound H2AK13Cub-NCP cryo-EM map. Molecular graphics images were produced using the UCSF Chimera package(109).

Figure Supplements

Figure 1-figure supplement 1. A. Pull-down assays of NCP ubiquitylated by RNF168 using either MBP-RNF169(UDM2) or MBP-RNF168(UDM2) in the presence of varying concentrations of the acidic patch interacting KSHV LANA peptide. In addition the 8LRS10 mutant (mut: L8A R9A and S10A) that does not bind the NCP is added in 1 case (concentration of the LANA peptide in μM). **B.** Pull-down assay of NCPs conjugated to ubiquitin with MBP-RNF169(UDM2). H2A mutants K15R and K13R were used to catalytically produce monoubiquitylated H2AK13-ub and H2AK15-ub, respectively. Catalytic ubiquitylation of K13R and K15R species by RNF168 produces a small amount of diubiquitylated H2A with the second ubiquitin conjugated to position K36, as indicated on the gel (13). Input: 5% of the amount of ubiquitylated NCPs used in pull-down; the migration of molecular mass markers (kDa) is indicated on the left.

Figure 2-figure supplement 1. A. Primary sequence of the modified RNF169(UDM2) construct used for NMR experiments at 45°C; addition of four N-terminal residues shown in bold. **B.** Temperature melt of wild-type RNF169(UDM2) and the N-terminal extended variant using circular dichroism spectroscopy. Helical percentage calculated as described in Materials and Methods.

Figure 3-figure supplement 1. A. Schematic outlining the chemical activation of H2AK13C and conjugation with ubG76C. **B.** NMR derived diffusion constants for free ubiquitin (black), H2AK13Cub-NCP (red) and ¼ proteasome (green). Plot of $1/T\ln(I/I_o)$ as a function of squared gradient strength (circles), where T is the diffusion time (100 ms for ubiquitin, 250 ms for NCP and ¼ proteasome) and I, I_o are the intensities in the presence and absence of encoding gradients, with best fits (lines) and calculated diffusion constants indicated. **C.** Pull-down assays of NCPs ubiquitylated by RNF168 (ub_{CAT}) or prepared through the disulfide directed approach (K13C-Ub_{ss}). MBP-RNF169(UDM2) was used in the pull-down. One pull-down in the absence of RNF168 (- E3-ligase) is used as a negative control. The gel was run in the presence of a reducing agent (dithiothreitol) so the H2AK13C-Ubss linkage is reduced to H2AK13C. Antibody against the acidic patch of H2A was used to detect H2A from Drosophila. Catalytic ubiquitylation of K15C species by RNF168 produces a small amount of diubiquitylated H2A with the second ubiquitin conjugated to position K36, as indicated on the gel (13). The * indicates an artifact from the gel. Input: 5% of the amount of ubiquitylated NCPs used in pull-down. The migration of molecular mass markers (kDa) is indicated on the right.

Figure 3-figure supplement 2. A. Overlay of ^{1}H-^{13}C HMQC spectra of ILV-methyl labeled ubiquitin with increasing amounts of RNF169(UDM2), as indicated. Data recorded at 11.7 T, 45°C. Final RNF169(UDM2) to ubiquitin ratio of 42:1. **B.** Pull-down assay of NCPs conjugated to wild-type or I44A ubiquitin with MBP-RNF169(UDM2) (top panel) or MBP-RNF168(UDM2). Ub-NCP binding-deficient RNF169(L699A/R700A) and RNF168(L476A/R477A) mutants, denoted by LR, were used as negative controls. Input: 5% of the amount of ubiquitylated NCPs used in pull-down; the migration of molecular mass markers (kDa) is indicated on the left.

Figure 3-figure supplement 3. Selected regions of CT-^{1}H-^{13}C HSQC spectra of ^{15}N,^{13}C wild-type RNF169(UDM2) with increasing amounts of unlabeled ubiquitin. Arrows indicate direction of peak movement. Data collected at 11.7 T, 35°C.

Figure 4-figure supplement 1. Overlay of ^{1}H-^{13}C HMQC spectra of ILV-methyl labeled H3 H2AK13Cub-NCPs with (red) and without (black) RNF169(UDM2). No significant CSPs are observed. Data recorded at 14.1 T, 45^{o}C.

Figure 5-figure supplement 1. A. Quantification of 53BP1 foci in U2OS cells transfected with GFP-RNF169(UDM2) wild-type or mutant, as indicated along the horizontal axis. CTRL: untransfected cells, LARA: L699A/R700A. Error bars represent the mean ± 1 standard deviaton for n = 3. Cells were irradiated (2 Gy) and processed for 53BP1 and γ-H2AX immunofluorescence as well as GFP imaging 1 hour after irradiation. **B.** Corresponding micrographs of the experiments presented in **A**. Dash lines outline nucleus of the cells and scale bar represents 5 μm.

Figure 5-figure supplement 2. ^{1}H-^{13}C CT-HSQC of ^{15}N,^{13}C wild-type RNF169(UDM2). Significant resonance overlap of leucine residues is observed. Data recorded at 11.7 T, 35C°.

Figure 5-figure supplement 3. A. Alignment of the primary sequences of RNF169(UDM2) and the LANA peptide. Common residues that have been shown to be relevant for NCP binding are shaded in gray. **B.** Selected regions of ^{1}H-^{13}C HMQC spectra of free ILV-methyl labeled H2B in the context of H2AK13Cub-NCPs in black, overlaid with corresponding spectral regions as recorded on ILV-methyl labeled H2B H2AK13Cub-NCP samples with RNF169(UDM2) (red), with the LANA peptide (purple), with RNF169(R689/R690/K691A)(UDM2) (blue) and with RNF169(L699/R700/S701A)(UDM2) (green). Residues with significant CSPs are labeled, and the ratio of RNF169(UDM2) or LANA to ubiquitin was 5:1. All spectra were recorded at 14.1 T, 45°C.

Figure 7-figure supplement 1. **A**. Representative cryo-EM micrographs. Several individual particle projections are boxed. **B**. Examples of 2D class average images from cryo-EM of the RNF169(UDM2)-ubNCP complex. **C**. 3D classification of the 90 200 selected particle images obtained after 2D classification. All classes show varying detail, location and volume of density for the covalently attached ubiquitin. The most populated high-resolution class was refined with C2 symmetry to yield the final RNF169(UDM2)-ubNCP map. **D**. Fourier shell correlation curve after

a gold-standard map refinement of the ubNCP structure obtained during preliminary complex optimization, corrected for the effects of map masking. **E**. Fourier shell correlation curve after a gold-standard map refinement of the final RNF169(UDM2)-ubNCP structure, corrected for the effects of map masking. **F**. Euler angle distribution plot of all particle images used for the symmetrized ubNCP map. Bar length and color (blue low, red high) corresponds to number of particle images contributing to each view. **G**. Euler angle distribution plot of all particle images used for the symmetrized RNF169(UDM2)-ubNCP map. Bar length and color (blue low, red high) corresponds to number of particle images contributed to each view.

Figure 8-figure supplement 1. Schematic outline of replica-averaged MD protocol used. Restraints used in each stage are indicated in boxes; COM: centre of mass, CS: chemical shifts, NOEs: Nuclear Overhauser effects, contacts: CSPs and mutagenesis restraints. Temperature and timescale of each step is indicated above arrows. Explicit details can be found in Materials and Methods.

Figure 8-figure supplement 2. Initial position of ub in RNF(UDM2)-ubNCP starting structures does not influence the final ub orientation. **A.** Alignment of RNF(UDM2)-ubNCP starting conformations for replica-averaged MD simulations. Histones H2A and H2B were used to align the structures with only one copy of the histones and DNA shown for simplicity. The starting

position of ubiquitin used in a pair of simulations is shown in black and red. RNF169(662-682)(MIU2): orange, RNF169(683-708)(LRM2): blue, H2A: light yellow, H2B: salmon, H3: light blue, H4: light green, DNA: gray. **B.** Alignment of RNF(UDM2)-ubNCP final conformations from replica-averaged MD simulations, as in A.

REFERENCES

1. Komander D & Rape M (2012) The ubiquitin code. *Annu Rev Biochem* 81:203-229.
2. Jackson SP & Durocher D (2013) Regulation of DNA damage responses by ubiquitin and SUMO. *Mol Cell* 49(5):795-807.
3. Dikic I, Wakatsuki S, & Walters KJ (2009) Ubiquitin-binding domains - from structures to functions. *Nat Rev Mol Cell Bio* 10(10):659-671.
4. Hicke L, Schubert HL, & Hill CP (2005) Ubiquitin-binding domains. *Nature reviews. Molecular cell biology* 6(8):610-621.
5. Panier S, Ichijima Y, Fradet-Turcotte A, Leung CCY, Kaustov L, Arrowsmith CH, & Durocher D (2012) Tandem Protein Interaction Modules Organize the Ubiquitin-Dependent Response to DNA Double-Strand Breaks. *Molecular Cell* 47(3):383-395.

6. Panier S & Durocher D (2013) Push back to respond better: regulatory inhibition of the DNA double-strand break response. *Nat Rev Mol Cell Bio* 14(10):661-672.
7. Thorslund T, Ripplinger A, Hoffmann S, Wild T, Uckelmann M, Villumsen B, Narita T, Sixma TK, Choudhary C, Bekker-Jensen S, & Mailand N (2015) Histone H1 couples initiation and amplification of ubiquitin signalling after DNA damage. *Nature* 527(7578):389-+.
8. Gatti M, Pinato S, Maspero E, Soffientini P, Polo S, & Penengo L (2012) A novel ubiquitin mark at the N-terminal tail of histone H2As targeted by RNF168 ubiquitin ligase. *Cell Cycle* 11(13):2538-2544.
9. Mattiroli F, Vissers JHA, van Dijk WJ, Ikpa P, Citterio E, Vermeulen W, Marteijn JA, & Sixma TK (2012) RNF168 Ubiquitinates K13-15 on H2A/H2AX to Drive DNA Damage Signaling. *Cell* 150(6):1182-1195.
10. Chen J, Feng WJ, Jiang J, Deng YQ, & Huen MSY (2012) Ring Finger Protein RNF169 Antagonizes the Ubiquitin-dependent Signaling Cascade at Sites of DNA Damage. *Journal of Biological Chemistry* 287(33):27715-27722.
11. Poulsen M, Lukas C, Lukas J, Bekker-Jensen S, & Mailand N (2012) Human RNF169 is a negative regulator of the ubiquitin-dependent response to DNA double-strand breaks. *J Cell Biol* 197(2):189-199.
12. Fradet-Turcotte A, Canny MD, Escribano-Diaz C, Orthwein A, Leung CC, Huang H, Landry MC, Kitevski-LeBlanc J, Noordermeer SM, Sicheri F, & Durocher D (2013) 53BP1 is a reader of the DNA-damage-induced H2A Lys 15 ubiquitin mark. *Nature* 499(7456):50-54.
13. Wilson MD, Benlekbir S, Fradet-Turcotte A, Sherker A, Julien JP, McEwan A, Noordermeer SM, Sicheri F, Rubinstein JL, & Durocher D (2016) The structural basis of modified nucleosome recognition by 53BP1. *Nature* 536(7614):100-103.
14. Sprangers R & Kay LE (2007) Quantitative dynamics and binding studies of the 20S proteasome by NMR. in *Nature*, pp 618-622.
15. Rosenzweig R & Kay LE (2014) Bringing Dynamic Molecular Machines into Focus by Methyl-TROSY NMR. *Annu Rev Biochem* 83:291-315.
16. Gelis I, Bonvin AM, Keramisanou D, Koukaki M, Gouridis G, Karamanou S, Economou A, & Kalodimos CG (2007) Structural basis for signal-sequence recognition by the translocase motor SecA as determined by NMR. *Cell* 131(4):756-769.
17. Cavalli A, Camilloni C, & Vendruscolo M (2013) Molecular dynamics simulations with replica-averaged structural restraints generate structural ensembles according to the maximum entropy principle. *The Journal of chemical physics* 138(9):094112.
18. Cao J & Yan Q (2012) Histone ubiquitination and deubiquitination in transcription, DNA damage response, and cancer. *Frontiers in oncology* 2:26.
19. Wang HB, Wang LJ, Erdjument-Bromage H, Vidal M, Tempst P, Jones RS, & Zhang Y (2004) Role of histone H2A ubiquitination in polycomb silencing. *Nature* 431(7010):873-878.
20. Sattler M, Schleucher J, & Griesinger C (1999) Heteronuclear multidimensional NMR experiments for the structure determination of proteins in solution employing pulsed field gradients. *Progress in Nuclear Magnetic Resonance Spectroscopy* 34(2):93-158.

21. Marsh JA, Singh VK, Jia ZC, & Forman-Kay JD (2006) Sensitivity of secondary structure propensities to sequence differences between alpha- and gamma-synuclein: Implications for fibrillation. *Protein Science* 15(12):2795-2804.
22. Berjanskii MV & Wishart DS (2005) A simple method to predict protein flexibility using secondary chemical shifts. *J Am Chem Soc* 127(43):14970-14971.
23. Lipari G & Szabo A (1982) Model-Free Approach to the Interpretation of Nuclear Magnetic-Resonance Relaxation in Macromolecules .1. Theory and Range of Validity. *Journal of the American Chemical Society* 104(17):4546-4559.
24. Penengo L, Mapelli M, Murachelli AG, Confalonieri S, Magri L, Musacchio A, Di Fiore PP, Polo S, & Schneider TR (2006) Crystal structure of the ubiquitin binding domains of rabex-5 reveals two modes of interaction with ubiquitin. *Cell* 124(6):1183-1195.
25. Dyer PN, Edayathumangalam RS, White CL, Bao YH, Chakravarthy S, Muthurajan UM, & Luger K (2004) Reconstitution of nucleosome core particles from recombinant histones and DNA. *Method Enzymol* 375:23-44.
26. Choy WY, Mulder FAA, Crowhurst KA, Muhandiram DR, Millett IS, Doniach S, Forman-Kay JD, & Kay LE (2002) Distribution of molecular size within an unfolded state ensemble using small-angle X-ray scattering and pulse field gradient NMR techniques. *Journal of Molecular Biology* 316(1):101-112.
27. Religa TL, Sprangers R, & Kay LE (2010) Dynamic regulation of archaeal proteasome gate opening as studied by TROSY NMR. in *Science*, pp 98-102.
28. Hurley JH, Lee S, & Prag G (2006) Ubiquitin-binding domains. *Biochem J* 399:361-372.
29. Chen ZJJ & Sun LJJ (2009) Nonproteolytic Functions of Ubiquitin in Cell Signaling. *Molecular Cell* 33(3):275-286.
30. Tugarinov V & Kay LE (2003) Quantitative NMR studies of high molecular weight proteins: application to domain orientation and ligand binding in the 723 residue enzyme malate synthase G. *J Mol Biol* 327(5):1121-1133.
31. Alsallaq R & Zhou HX (2007) Prediction of protein-protein association rates from a transition-state theory. *Structure* 15(2):215-224.
32. Schlosshauer M & Baker D (2004) Realistic protein-protein association rates from a simple diffusional model neglecting long-range interactions, free energy barriers, and landscape ruggedness. *Protein Science* 13(6):1660-1669.
33. Tugarinov V, Hwang PM, Ollerenshaw JE, & Kay LE (2003) Cross-correlated relaxation enhanced 1H[bond]13C NMR spectroscopy of methyl groups in very high molecular weight proteins and protein complexes. in *J Am Chem Soc*, pp 10420-10428.
34. Kato H, van Ingen H, Zhou BR, Feng HQ, Bustin M, Kay LE, & Bai YW (2011) Architecture of the high mobility group nucleosomal protein 2-nucleosome complex as revealed by methyl-based NMR. *Proceedings of the National Academy of Sciences of the United States of America* 108(30):12283-12288.
35. Kalashnikova AA, Porter-Goff ME, Muthurajan UM, Luger K, & Hansen JC (2013) The role of the nucleosome acidic patch in modulating higher order chromatin structure. *J R Soc Interface* 10(82).

36. Barbera AJ, Chodaparambil JV, Kelley-Clarke B, Joukov V, Walter JC, Luger K, & Kaye KM (2006) The nucleosomal surface as a docking station for Kaposi's sarcoma herpesvirus LANA. *Science* 311(5762):856-861.
37. McGinty RK, Henrici RC, & Tan S (2014) Crystal structure of the PRC1 ubiquitylation module bound to the nucleosome. *Nature* 514(7524):591-+.
38. Makde RD, England JR, Yennawar HP, & Tan S (2010) Structure of RCC1 chromatin factor bound to the nucleosome core particle. *Nature* 467(7315):562-U581.
39. Armache KJ, Garlick JD, Canzio D, Narlikar GJ, & Kingston RE (2011) Structural Basis of Silencing: Sir3 BAH Domain in Complex with a Nucleosome at 3.0 angstrom Resolution. *Science* 334(6058):977-982.
40. Morgan MT, Haj-Yahya M, Ringel AE, Bandi P, Brik A, & Wolberger C (2016) Structural basis for histone H2B deubiquitination by the SAGA DUB module. *Science* 351(6274):725-728.
41. McGinty RK & Tan S (2015) Nucleosome Structure and Function. *Chemical Reviews* 115(6):2255-2273.
42. Dominguez C, Boelens R, & Bonvin AMJJ (2003) HADDOCK: A protein-protein docking approach based on biochemical or biophysical information. *Journal of the American Chemical Society* 125(7):1731-1737.
43. Bai XC, Yan C, Yang G, Lu P, Ma D, Sun L, Zhou R, Scheres SH, & Shi Y (2015) An atomic structure of human gamma-secretase. *Nature* 525(7568):212-217.
44. Smith MTJ & Rubinstein JL (2014) Structural Biology Beyond Blob-Ology. *Science* 345(6197):617-619.
45. Khoshouei M, Radjainia, M., Baumeister, W., Danev, R. (2016) Cryo-EM structure of haemoglobin at 3.2A determined with Volta phase plate. *in press*.
46. Clapier CR, Chakravarthy S, Petosa C, Fernández-Tornero C, Luger K, & Müller CW (2008) Structure of the Drosophila nucleosome core particle highlights evolutionary constraints on the H2A-H2B histone dimer. in *Proteins*, pp 1-7.
47. Kucukelbir A, Sigworth FJ, & Tagare HD (2014) Quantifying the local resolution of cryo-EM density maps. *Nature methods* 11(1):63-65.
48. Sun H, Kay LE, & Tugarinov V (2011) An optimized relaxation-based coherence transfer NMR experiment for the measurement of side-chain order in methyl-protonated, highly deuterated proteins. *The journal of physical chemistry. B* 115(49):14878-14884.
49. Kukic P, Camilloni C, Cavalli A, & Vendruscolo M (2014) Determination of the Individual Roles of the Linker Residues in the Interdomain Motions of Calmodulin Using NMR Chemical Shifts. *Journal of Molecular Biology* 426(8):1826-1838.
50. Kukic P, Lundstrom P, Camilloni C, Evenas J, Akke M, & Vendruscolo M (2016) Structural Insights into the Calcium-Mediated Allosteric Transition in the C-Terminal Domain of Calmodulin from Nuclear Magnetic Resonance Measurements. *Biochemistry* 55(1):19-28.
51. Gardner KH & Kay LE (1997) Production and incorporation of N-15, C-13, H-2 (H-1-delta 1 methyl) isoleucine into proteins for multidimensional NMR studies. *Journal of the American Chemical Society* 119(32):7599-7600.

52. Goto NK, Gardner KH, Mueller GA, Willis RC, & Kay LE (1999) A robust and cost-effective method for the production of Val, Leu, Ile (delta 1) methyl-protonated N-15-, C-13-, H-2-labeled proteins. *J Biomol Nmr* 13(4):369-374.
53. Tugarinov V & Kay LE (2004) An isotope labeling strategy for methyl TROSY spectroscopy. *J Biomol Nmr* 28(2):165-172.
54. Kainosho M, Torizawa T, Iwashita Y, Terauchi T, Mei Ono A, & Guntert P (2006) Optimal isotope labelling for NMR protein structure determinations. *Nature* 440(7080):52-57.
55. Fiaux J, Bertelsen EB, Horwich AL, & Wuthrich K (2002) NMR analysis of a 900K GroEL GroES complex. *Nature* 418(6894):207-211.
56. Janin J, Miller S, & Chothia C (1988) Surface, subunit interfaces and interior of oligomeric proteins. *J Mol Biol* 204(1):155-164.
57. Battiste JL & Wagner G (2000) Utilization of site-directed spin labeling and high-resolution heteronuclear nuclear magnetic resonance for global fold determination of large proteins with limited nuclear overhauser effect data. *Biochemistry* 39(18):5355-5365.
58. Wüthrich K (1986) *NMR of proteins and nucleic acids* (Wiley, New York) pp xv, 292 p.
59. Mittag T & Forman-Kay JD (2007) Atomic-level characterization of disordered protein ensembles. *Curr Opin Struc Biol* 17(1):3-14.
60. Vendruscolo M & Dobson CM (2011) Protein dynamics: Moore's law in molecular biology. *Current biology : CB* 21(2):R68-70.
61. Chung HS, Piana-Agostinetti S, Shaw DE, & Eaton WA (2015) Structural origin of slow diffusion in protein folding. *Science* 349(6255):1504-1510.
62. Torda AE, Scheek RM, & Vangunsteren WF (1989) Time-Dependent Distance Restraints in Molecular-Dynamics Simulations. *Chem Phys Lett* 157(4):289-294.
63. Lindorff-Larsen K, Best RB, Depristo MA, Dobson CM, & Vendruscolo M (2005) Simultaneous determination of protein structure and dynamics. *Nature* 433(7022):128-132.
64. Cavalli A, Camilloni C, & Vendruscolo M (2013) Molecular dynamics simulations with replica-averaged structural restraints generate structural ensembles according to the maximum entropy principle (vol 138, 094112, 2013). *Journal of Chemical Physics* 139(16).
65. Kato H, Jiang J, Zhou B-R, Rozendaal M, Feng H, Ghirlando R, Xiao TS, Straight AF, & Bai Y (2013) A Conserved Mechanism for Centromeric Nucleosome Recognition by Centromere Protein CENP-C. in *Science*, pp 1110-1113.
66. Juang YC, Landry MC, Sanches M, Vittal V, Leung C, Ceccarelli DF, Mateo ARF, Pruneda JN, Mao D, Szilard RK, Orlicky S, Munro M, Brzovic PS, Klevit RE, Sicheri F, & Durocher D (2012) OTUB1 Co-opts Lys48-Linked Ubiquitin Recognition to Suppress E2 Enzyme Function (vol 45, pg 384, 2012). *Molecular Cell* 46(4):549-549.
67. Kato H, van Ingen H, Zhou BR, Feng H, Bustin M, Kay LE, & Bai Y (2011) Architecture of the high mobility group nucleosomal protein 2-nucleosome complex as revealed by methyl-based NMR. *Proc Natl Acad Sci U S A* 108(30):12283-12288.

68. Malakhov MP, Mattern MR, Malakhova OA, Drinker M, Weeks SD, & Butt TR (2004) SUMO fusions and SUMO-specific protease for efficient expression and purification of proteins. *Journal of structural and functional genomics* 5(1-2):75-86.
69. Lowary PT & Widom J (1998) New DNA sequence rules for high affinity binding to histone octamer and sequence-directed nucleosome positioning. *J Mol Biol* 276(1):19-42.
70. Escribano-Diaz C, Orthwein A, Fradet-Turcotte A, Xing M, Young JT, Tkac J, Cook MA, Rosebrock AP, Munro M, Canny MD, Xu D, & Durocher D (2013) A cell cycle-dependent regulatory circuit composed of 53BP1-RIF1 and BRCA1-CtIP controls DNA repair pathway choice. *Mol Cell* 49(5):872-883.
71. Orthwein A, Noordermeer SM, Wilson MD, Landry S, Enchev RI, Sherker A, Munro M, Pinder J, Salsman J, Dellaire G, Xia B, Peter M, & Durocher D (2015) A mechanism for the suppression of homologous recombination in G1 cells. *Nature* 528(7582):422-426.
72. Sommese RF, Sivaramakrishnan S, Baldwin RL, & Spudich JA (2010) Helicity of short E-R/K peptides. *Protein Science* 19(10):2001-2005.
73. Chen YH, Yang JT, & Chau KH (1974) Determination of the helix and beta form of proteins in aqueous solution by circular dichroism. *Biochemistry* 13(16):3350-3359.
74. Delaglio F, Grzesiek S, Vuister GW, Zhu G, Pfeifer J, & Bax A (1995) NMRPipe: a multidimensional spectral processing system based on UNIX pipes. *J Biomol Nmr* 6(3):277-293.
75. Johnson BA & Blevins RA (1994) NMR View: A computer program for the visualization and analysis of NMR data. *J Biomol Nmr* 4(5):603-614.
76. Vranken WF, Boucher W, Stevens TJ, Fogh RH, Pajon A, Llinas M, Ulrich EL, Markley JL, Ionides J, & Laue ED (2005) The CCPN data model for NMR spectroscopy: development of a software pipeline. *Proteins* 59(4):687-696.
77. Cavanagh J (2007) Protein NMR spectroscopy principles and practice. (Academic Press, Amsterdam ; Boston), pp xxv, 885 p.
78. Muhandiram DR & Kay LE (1994) Gradient-Enhanced Triple-Resonance Three-Dimensional NMR Experiments with Improved Sensitivity. *Journal of Magnetic Resonance, Series B* 103(3):203-216.
79. Logan TM, Olejniczak ET, Xu RX, & Fesik SW (1993) A general method for assigning NMR spectra of denatured proteins using 3D HC(CO)NH-TOCSY triple resonance experiments. *J Biomol Nmr* 3(2):225-231.
80. Grzesiek S & Bax A (1992) Correlating Backbone Amide and Side-Chain Resonances in Larger Proteins by Multiple Relayed Triple Resonance Nmr. *Journal of the American Chemical Society* 114(16):6291-6293.
81. Neri D, Szyperski T, Otting G, Senn H, & Wuthrich K (1989) Stereospecific Nuclear Magnetic-Resonance Assignments of the Methyl-Groups of Valine and Leucine in the DNA-Binding Domain of the 434-Repressor by Biosynthetically Directed Fractional C-13 Labeling. *Biochemistry* 28(19):7510-7516.
82. Vuister GW & Bax A (1992) Resolution Enhancement and Spectral Editing of Uniformly C-13-Enriched Proteins by Homonuclear Broad-Band C-13 Decoupling. *J. Magn. Reson.* 98(2):428-435.

83. Santoro J & King GC (1992) A Constant-Time 2d Overbodenhausen Experiment for Inverse Correlation of Isotopically Enriched Species. *J. Magn. Reson.* 97(1):202-207.
84. Wand AJ, Urbauer JL, McEvoy RP, & Bieber RJ (1996) Internal dynamics of human ubiquitin revealed by 13C-relaxation studies of randomly fractionally labeled protein. *Biochemistry* 35(19):6116-6125.
85. Marr CR, Benlekbir S, & Rubinstein JL (2014) Fabrication of carbon films with approximately 500nm holes for cryo-EM with a direct detector device. *Journal of structural biology* 185(1):42-47.
86. Russo CJ & Passmore LA (2014) Electron microscopy: Ultrastable gold substrates for electron cryomicroscopy. *Science* 346(6215):1377-1380.
87. Rubinstein JL & Brubaker MA (2015) Alignment of cryo-EM movies of individual particles by optimization of image translations. *Journal of structural biology* 192(2):188-195.
88. Rohou A & Grigorieff N (2015) CTFFIND4: Fast and accurate defocus estimation from electron micrographs. *Journal of structural biology* 192(2):216-221.
89. Scheres SH (2012) RELION: implementation of a Bayesian approach to cryo-EM structure determination. *Journal of structural biology* 180(3):519-530.
90. Zhao J, Brubaker MA, Benlekbir S, & Rubinstein JL (2015) Description and comparison of algorithms for correcting anisotropic magnification in cryo-EM images. *Journal of structural biology* 192(2):209-215.
91. Davey CA, Sargent DF, Luger K, Maeder AW, & Richmond TJ (2002) Solvent mediated interactions in the structure of the nucleosome core particle at 1.9 angstrom resolution. *Journal of Molecular Biology* 319(5):1097-1113.
92. Rosenthal PB & Henderson R (2003) Optimal determination of particle orientation, absolute hand, and contrast loss in single-particle electron cryomicroscopy. *Journal of Molecular Biology* 333(4):721-745.
93. Fiser A & Sali A (2003) MODELLER: Generation and refinement of homology-based protein structure models. *Method Enzymol* 374:461-491.
94. Ivani I, Dans P, Noy A, Pérez A, Faustino I, Hospital A, Walther J, Andrio P, Goñi R, Balaceanu A, Portella G, Battistini F, Gelpí JL, González C, Vendruscolo M, Laughton C, Harris S, Case D, & Orozco M (2016) Parmbsc1: a refined force field for DNA simulations. *Nat Methods* 13(1):55-58.
95. Best R & Hummer G (2009) Optimized Molecular Dynamics Force Fields Applied to the Helix−Coil Transition of Polypeptides. *J. Phys. Chem. B* 113(26):9004–9015.
96. Jorgensen W, Chandrasekhar J, Madura J, Impey R, & Klein M (1983) Comparison of simple potential functions for simulating liquid water. *Journal of Chemical Physics* 79:926-935.
97. Pronk S, Páll S, Schulz R, Larsson P, Bjelkmar P, Apostolov R, Shirts M, Smith J, Kasson P, van der Spoel D, Hess B, & Lindahl E (2013) GROMACS 4.5: a high-throughput and highly parallel open source molecular simulation toolkit. *Bioinformatics* 29.

98. Tribello GA, Bonomi M, Branduardi D, Camilloni C, & Bussi G (2014) PLUMED 2: New feathers for an old bird. *Computer Physics Communications* 185(2):604-613.
99. Fu B, Sahakyan AB, Camilloni C, Tartaglia GG, Paci E, Caflisch A, Vendruscolo M, & Cavalli A (2014) ALMOST: An all atom molecular simulation toolkit for protein structure determination. *Journal of Computational Chemistry* 35(14):1101-1105.
100. Hess B, Kutzner C, van der Spoel D, & Lindahl E (2008) GROMACS 4: Algorithms for Highly Efficient, Load-Balanced, and Scalable Molecular Simulation. *Journal of Chemical Theory and Computation* 4(3):435-447.
101. Darden T, York D, & Pedersen L (1993) Particle mesh Ewald: An N⊕log(N) method for Ewald sums in large systems. *J. Chem. Phys.* 98.
102. van Zundert G, Rodrigues J, Trellet M, Schmitz C, Kastritis P, Karaca E, Melquiond A, van Dijk M, de Vries S, & Bonvin A (2016) The HADDOCK2.2 Web Server: User-Friendly Integrative Modeling of Biomolecular Complexes. *Journal of Molecular Biology* 484(4):720-725.
103. Fiser A, Do R, & Sali A (2000) Modeling of loops in protein structures. *Protein Science* 9(9):1753–1773.
104. Berendsen H, Postma J, van Gunsteren W, DiNola A, & Haak J (1984) Molecular dynamics with coupling to an external bath. *The Journal of Chemical Physics* 81.
105. Bussi G, Donadio D, & Parrinello M (2007) Canonical sampling through velocity rescaling. *The Journal of Chemical Physics* 126:014101.
106. Kukic P, Camilloni C, Cavalli A, & Vendruscolo M (2014) Determination of the Individual Roles of the Linker Residues in the Interdomain Motions of Calmodulin Using NMR Chemical Shifts. *Journal of Molecular Biology* 426(8):1826–1838.
107. Kohlhoff KJ, Robustelli P, Cavalli A, Salvatella X, & Vendruscolo M (2009) Fast and accurate predictions of protein NMR chemical shifts from interatomic distances. *J Am Chem Soc* 131(39):13894-13895.
108. Clapier CR, Chakravarthy S, Petosa C, Fernandez-Tornero C, Luger K, & Muller CW (2008) Structure of the Drosophila nucleosome core particle highlights evolutionary constraints on the H2A-H2B histone dimer. *Proteins* 71(1):1-7.
109. Pettersen EF, Goddard TD, Huang CC, Couch GS, Greenblatt DM, Meng EC, & Ferrin TE (2004) UCSF Chimera--a visualization system for exploratory research and analysis. *J Comput Chem* 25(13):1605-1612.

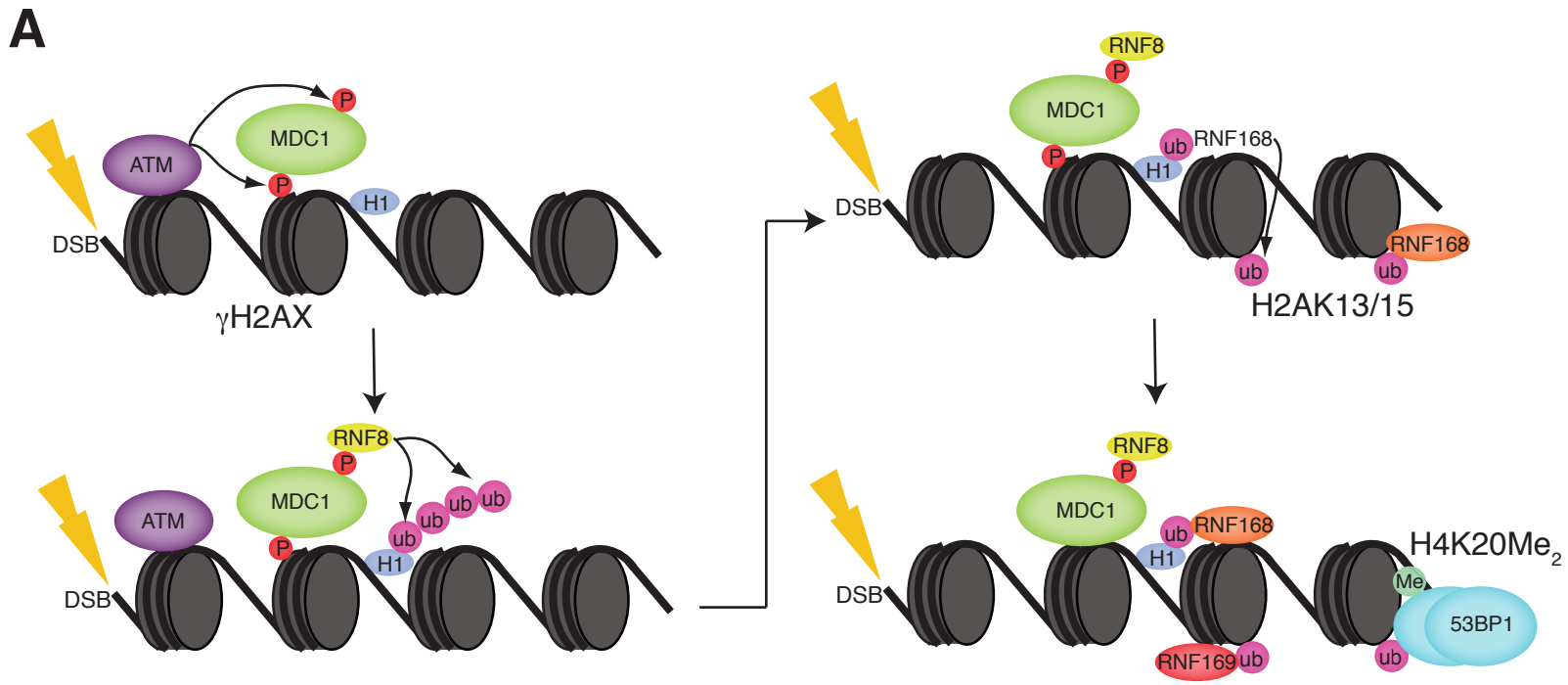
A
ATM
MDC1
P
H1
DSB
γH2AX
RNF8
ub
RNF168
H2AK13/15
RNF169
H4K20Me2
Me
53BP1

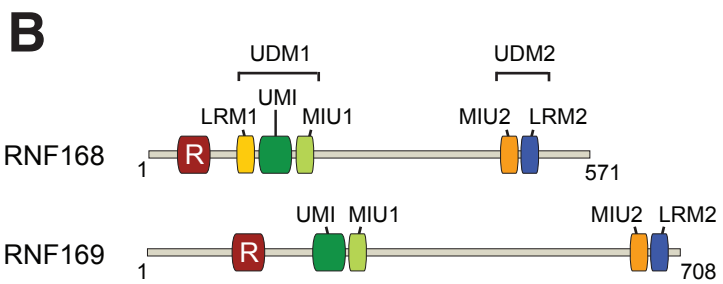
B
UDM1
UDM2
UMI
LRM1
MIU1
MIU2
LRM2
RNF168
R
1
571
RNF169
708

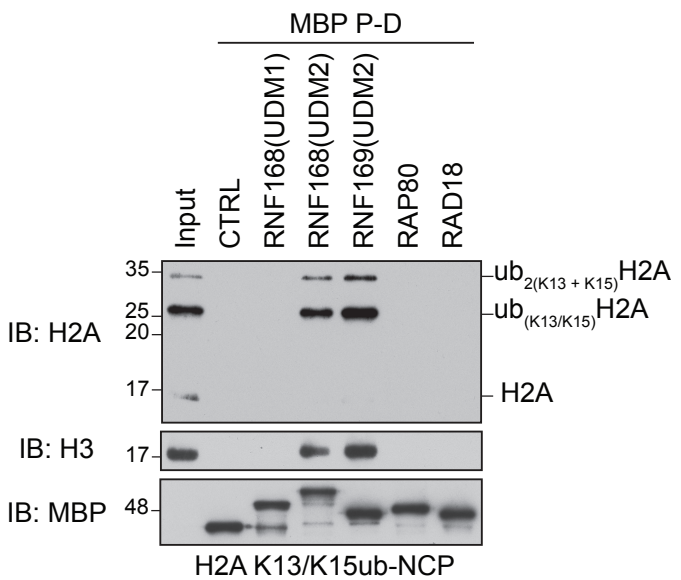
C
MBP P-D
Input
CTRL
RNF168(UDM1)
RNF168(UDM2)
RNF169(UDM2)
RAP80
RAD18
IB: H2A
IB: H3
IB: MBP
ub2(K13 + K15)H2A
ub(K13/K15)H2A
H2A
H2A K13/K15ub-NCP

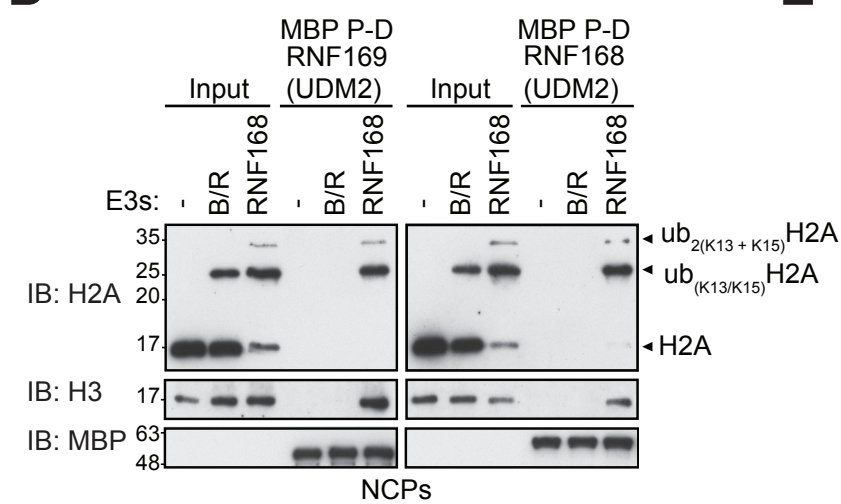
D
MBP P-D RNF169 (UDM2)
MBP P-D RNF168 (UDM2)
Input
E3s:
B/R
RNF168
IB: H2A
IB: H3
IB: MBP
ub2(K13 + K15)H2A
ub(K13/K15)H2A
H2A
NCPs

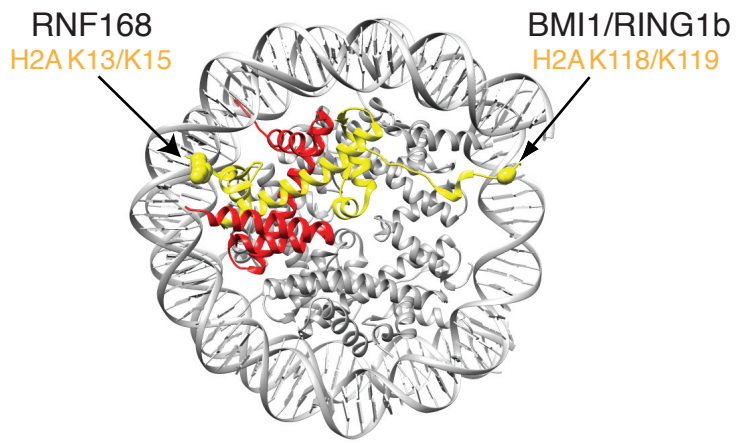
E
RNF168
H2A K13/K15
BMI1/RING1b
H2A K118/K119

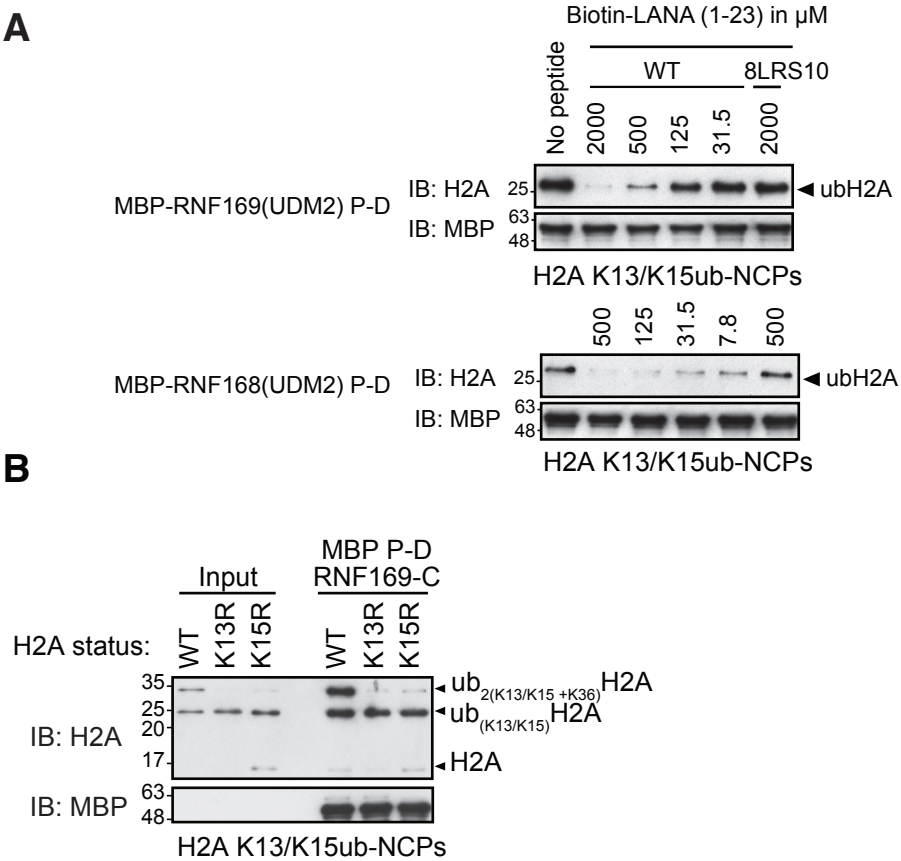
A
Biotin-LANA (1-23) in μM
No peptide
WT
8LRS10
2000
500
125
31.5
2000
MBP-RNF169(UDM2) P-D
IB: H2A
IB: MBP
25
63
48
ubH2A
H2A K13/K15ub-NCPs
500
125
31.5
7.8
500
MBP-RNF168(UDM2) P-D
IB: H2A
IB: MBP
25
63
48
ubH2A
H2A K13/K15ub-NCPs
B
Input
MBP P-D
RNF169-C
H2A status:
WT
K13R
K15R
WT
K13R
K15R
35
25
20
17
63
48
IB: H2A
IB: MBP
ub2(K13/K15 +K36)H2A
ub(K13/K15)H2A
H2A
H2A K13/K15ub-NCPs

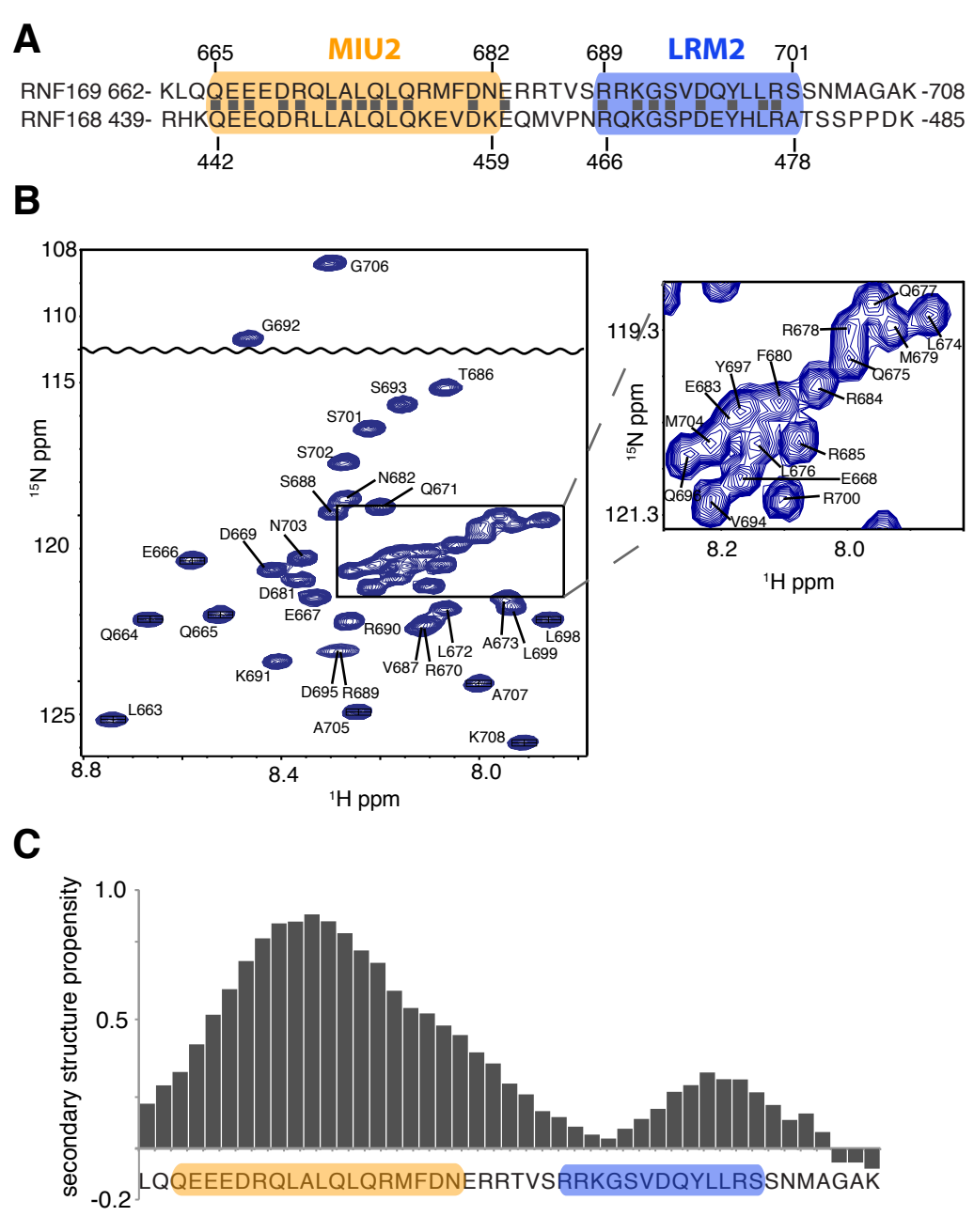
A
MIU2
LRM2
665
682
689
701
RNF169 662- KLQQEEEDRQLALQLQRMFDNERRTVSRRKGSVDQYLLRSSNMAGAK -708
RNF168 439- RHKQEEQDRLLALQLQKEVDKEQMVPNRQKGSPDEYHLRATSSPPDK -485
442
459
466
478
B
108
110
115
120
125
15N ppm
G706
G692
T686
S693
S701
S702
S688
N682
Q671
N703
D669
E666
D681
E667
Q664
Q665
R690
A673
L698
L672
L699
V687
R670
K691
D695
R689
A707
A705
L663
K708
8.8
8.4
8.0
1H ppm
119.3
121.3
Q677
R678
L674
M679
F680
Y697
Q675
E683
R684
M704
R685
L676
E668
Q696
R700
V694
8.2
8.0
C
secondary structure propensity
1.0
0.5
-0.2
LQQEEEDRQLALQLQRMFDNERRTVSRRKGSVDQYLLRSSNMAGAK

A

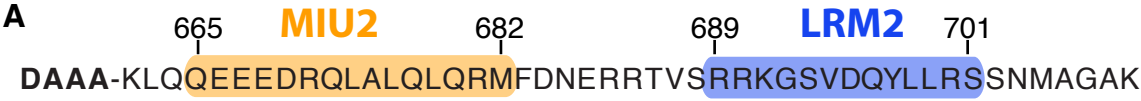
665
MIU2
682
689
LRM2
701
DAAA-KLQQEEEDRQLALQLQRMFDNERRTVSRRKGSVDQYLLRSSNMAGAK

B

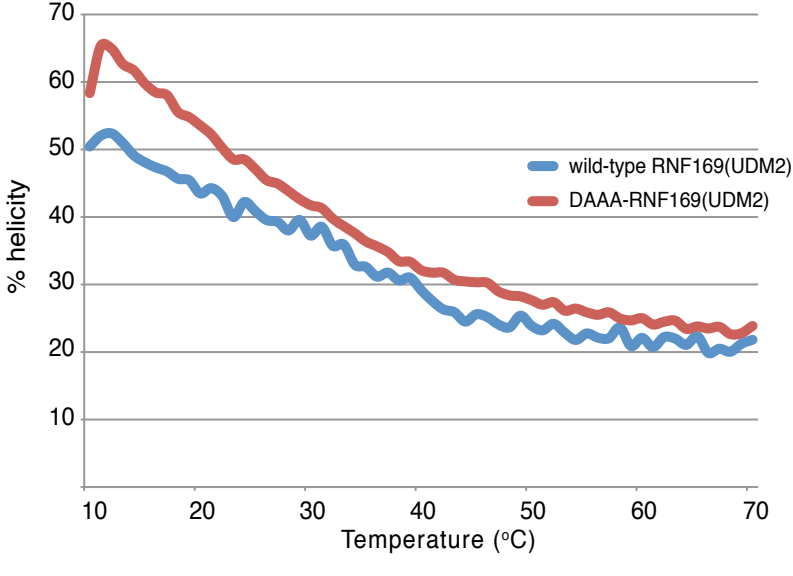
70
60
50
40
30
20
10
% helicity
wild-type RNF169(UDM2)
DAAA-RNF169(UDM2)
10
20
30
40
50
60
70
Temperature (°C)

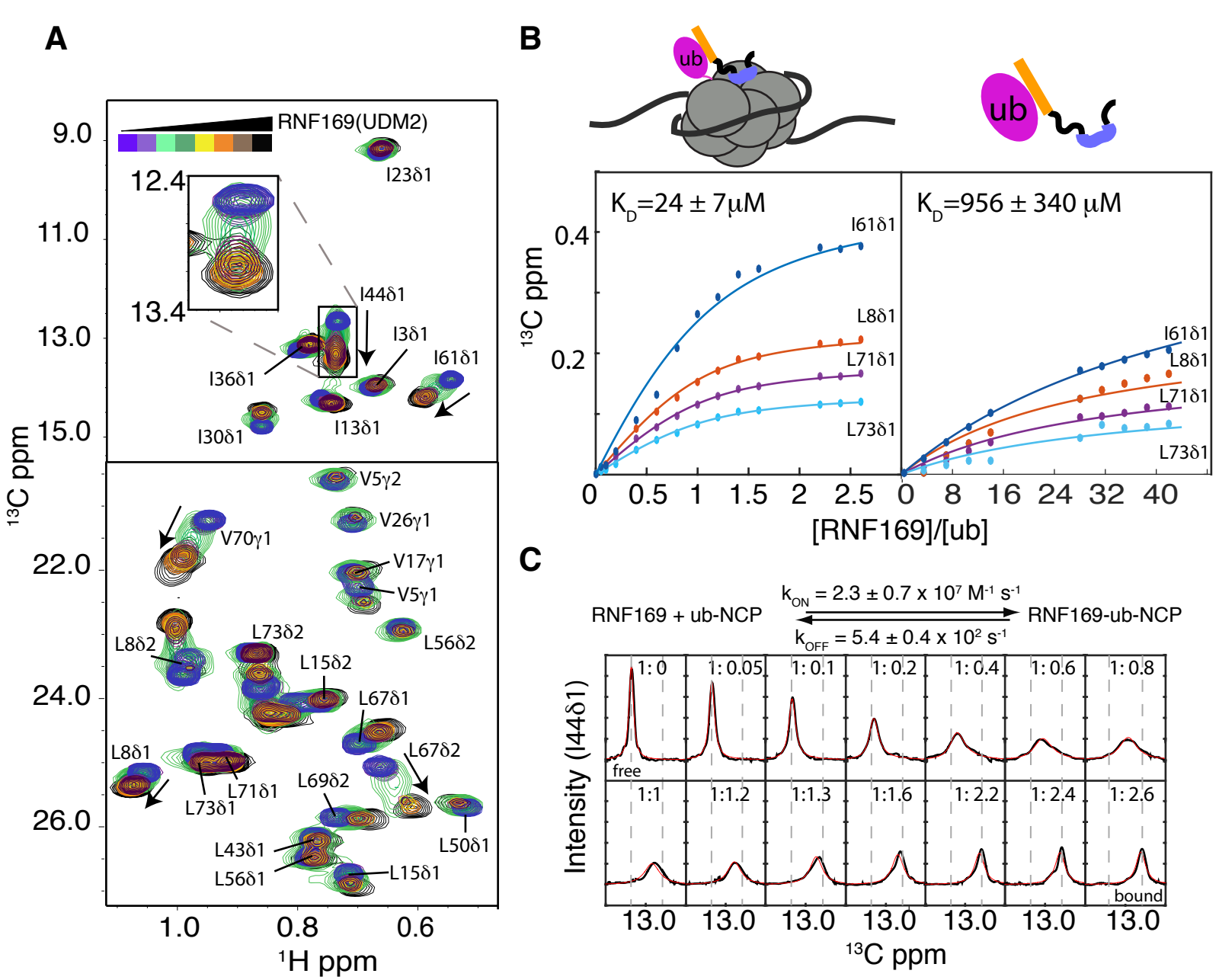
A
RNF169(UDM2)
I23δ1
I44δ1
I3δ1
I61δ1
I36δ1
I30δ1
I13δ1
V5γ2
V26γ1
V70γ1
V17γ1
V5γ1
L56δ2
L8δ2
L73δ2
L15δ2
L67δ1
L8δ1
L71δ1
L73δ1
L69δ2
L67δ2
L50δ1
L43δ1
L56δ1
L15δ1
^{13}C ppm
^{1}H ppm
B
ub
K_D=24 ± 7μM
K_D=956 ± 340 μM
I61δ1
L8δ1
L71δ1
L73δ1
^{13}C ppm
[RNF169]/[ub]
C
RNF169 + ub-NCP
RNF169-ub-NCP
k_{ON} = 2.3 ± 0.7 x 10^{7} M^{-1} s^{-1}
k_{OFF} = 5.4 ± 0.4 x 10^{2} s^{-1}
1: 0
1: 0.05
1: 0.1
1: 0.2
1: 0.4
1: 0.6
1: 0.8
free
1:1
1:1.2
1:1.3
1:1.6
1: 2.2
1: 2.4
1: 2.6
bound
Intensity (I44δ1)
^{13}C ppm

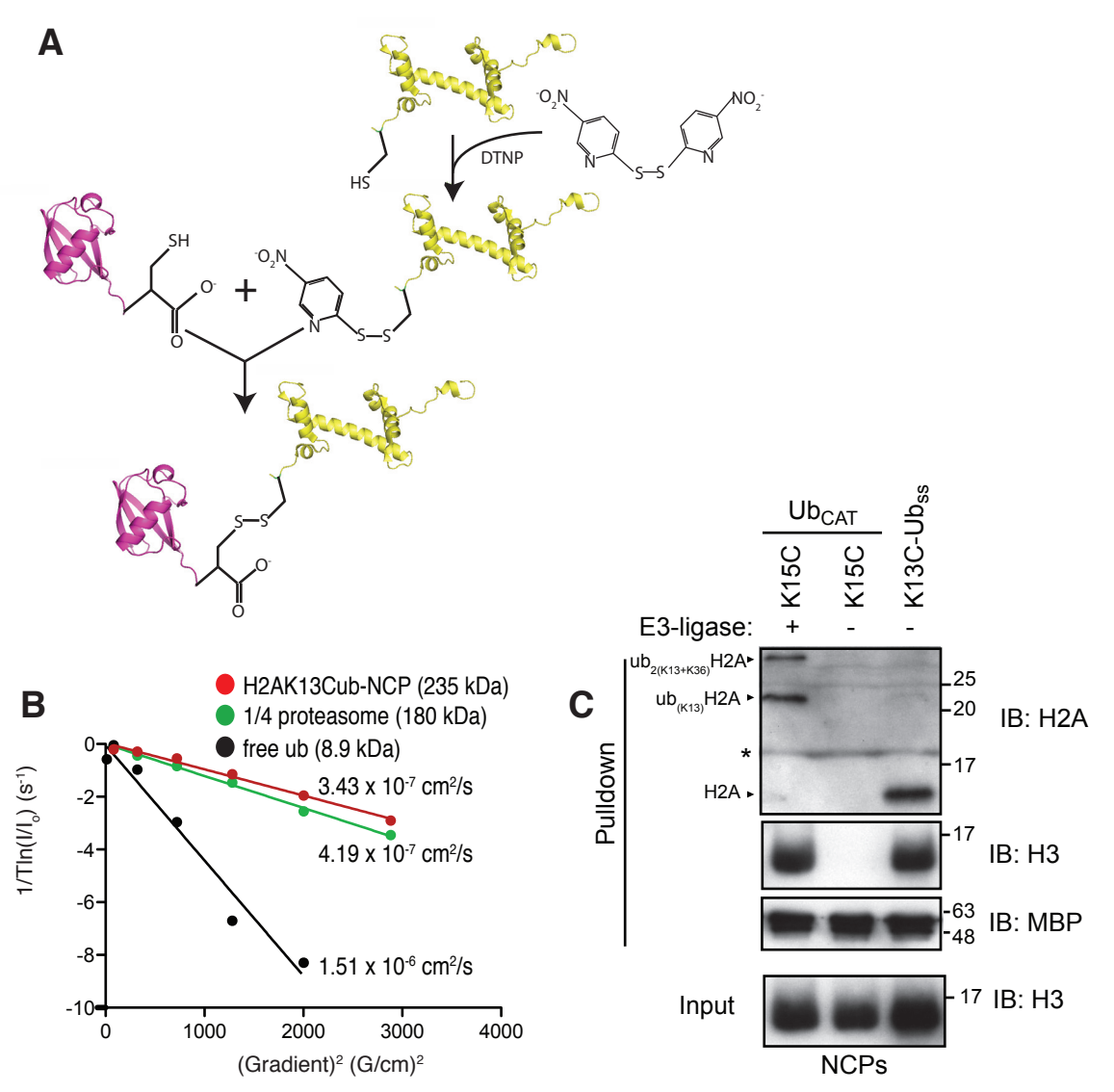
A
DTNP
HS
SH
B
H2AK13Cub-NCP (235 kDa)
1/4 proteasome (180 kDa)
free ub (8.9 kDa)
3.43 x 10-7 cm2/s
4.19 x 10-7 cm2/s
1.51 x 10-6 cm2/s
1/Tln(I/Io) (s-1)
(Gradient)2 (G/cm)2
C
UbCAT
K15C
K15C
K13C-Ubss
E3-ligase:
+
-
-
Pulldown
ub2(K13+K36) H2A
ub(K13) H2A
H2A
*
IB: H2A
IB: H3
IB: MBP
Input
IB: H3
NCPs

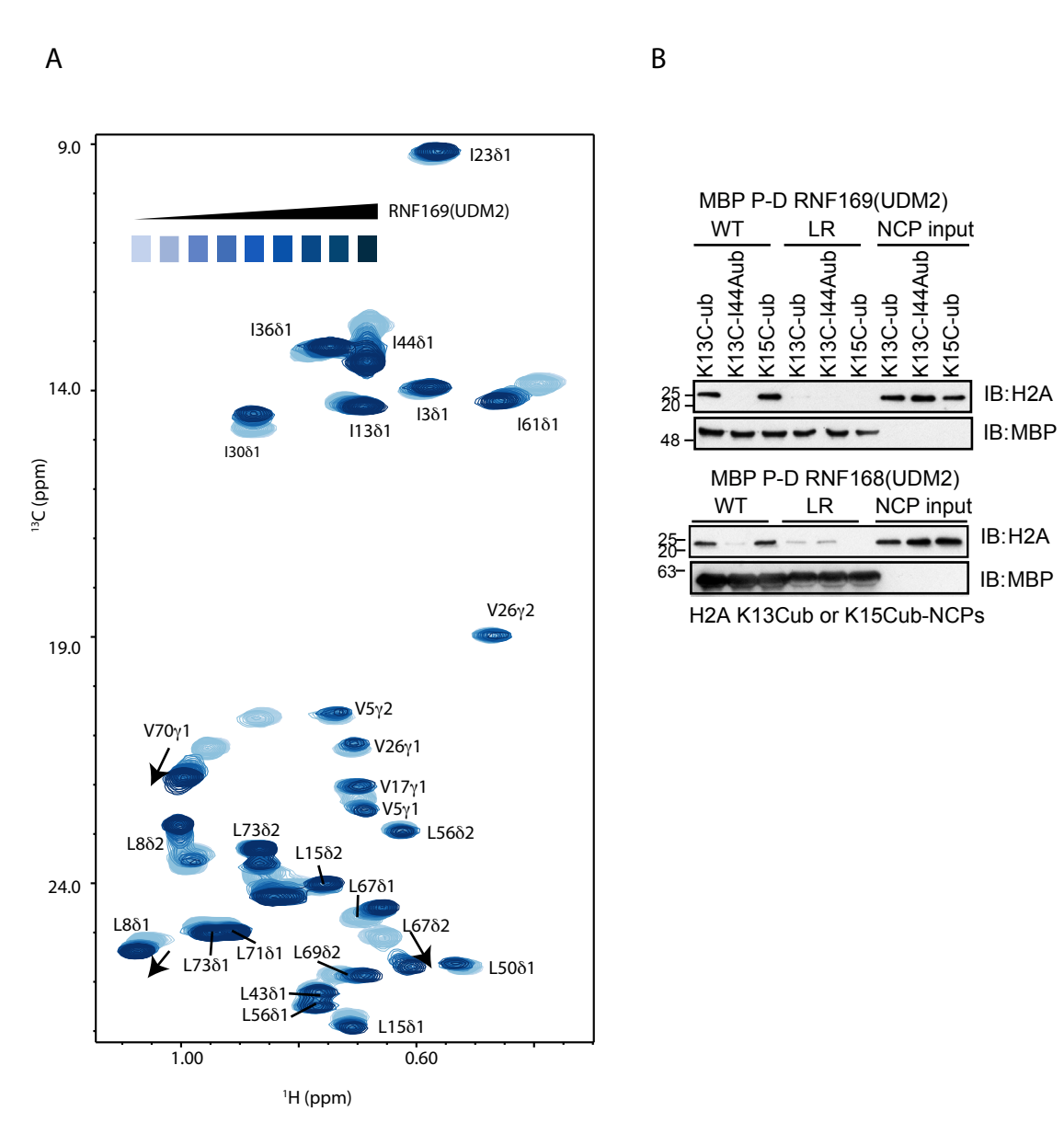
A
B
9.0
14.0
19.0
24.0
13C (ppm)
1.00
0.60
1H (ppm)
I23δ1
RNF169(UDM2)
I36δ1
I44δ1
I3δ1
I13δ1
I61δ1
I30δ1
V26γ2
V5γ2
V70γ1
V26γ1
V17γ1
V5γ1
L56δ2
L8δ2
L73δ2
L15δ2
L67δ1
L8δ1
L67δ2
L71δ1
L69δ2
L73δ1
L50δ1
L43δ1
L56δ1
L15δ1
MBP P-D RNF169(UDM2)
WT
LR
NCP input
K13C-ub
K13C-I44Aub
K15C-ub
K13C-ub
K13C-I44Aub
K15C-ub
K13C-ub
K13C-I44Aub
K15C-ub
25
20
48
IB:H2A
IB:MBP
MBP P-D RNF168(UDM2)
WT
LR
NCP input
25
20
63
IB:H2A
IB:MBP
H2A K13Cub or K15Cub-NCPs

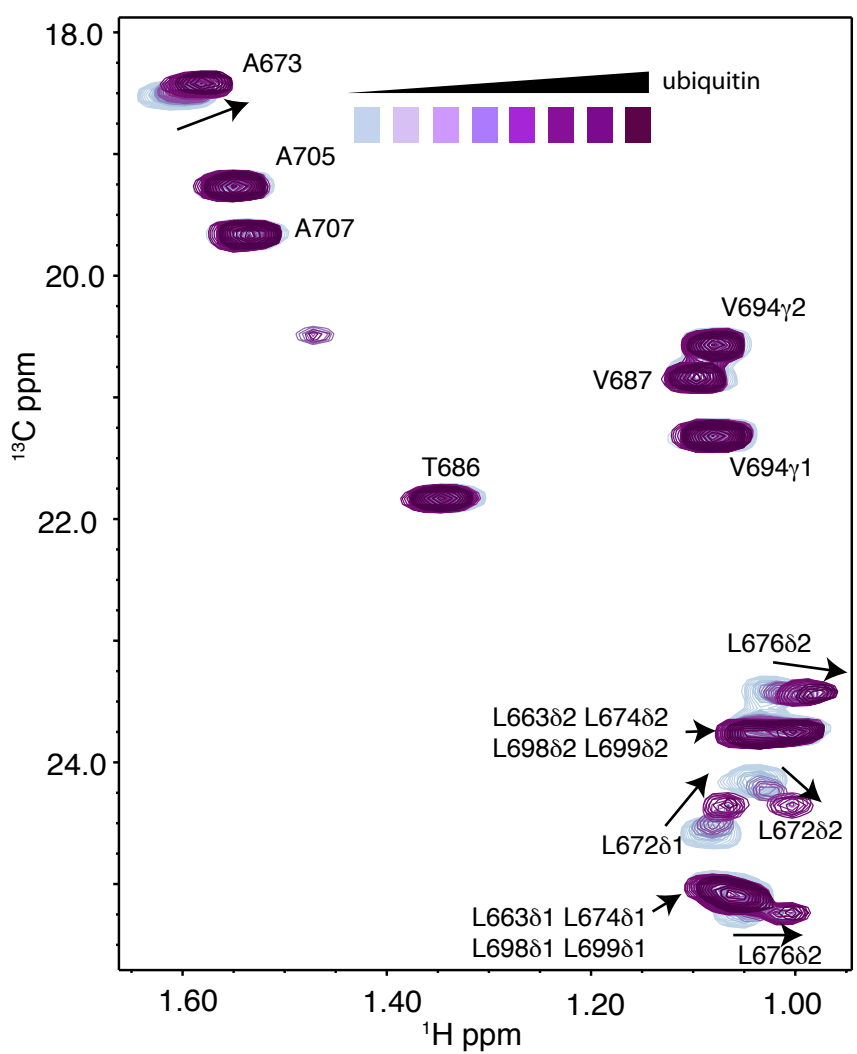
18.0
20.0
22.0
24.0
^{13}C ppm
1.60
1.40
1.20
1.00
^{1}H ppm
A673
ubiquitin
A705
A707
V694γ2
V687
V694γ1
T686
L676δ2
L663δ2 L674δ2
L698δ2 L699δ2
L672δ1
L672δ2
L663δ1 L674δ1
L698δ1 L699δ1
L676δ2

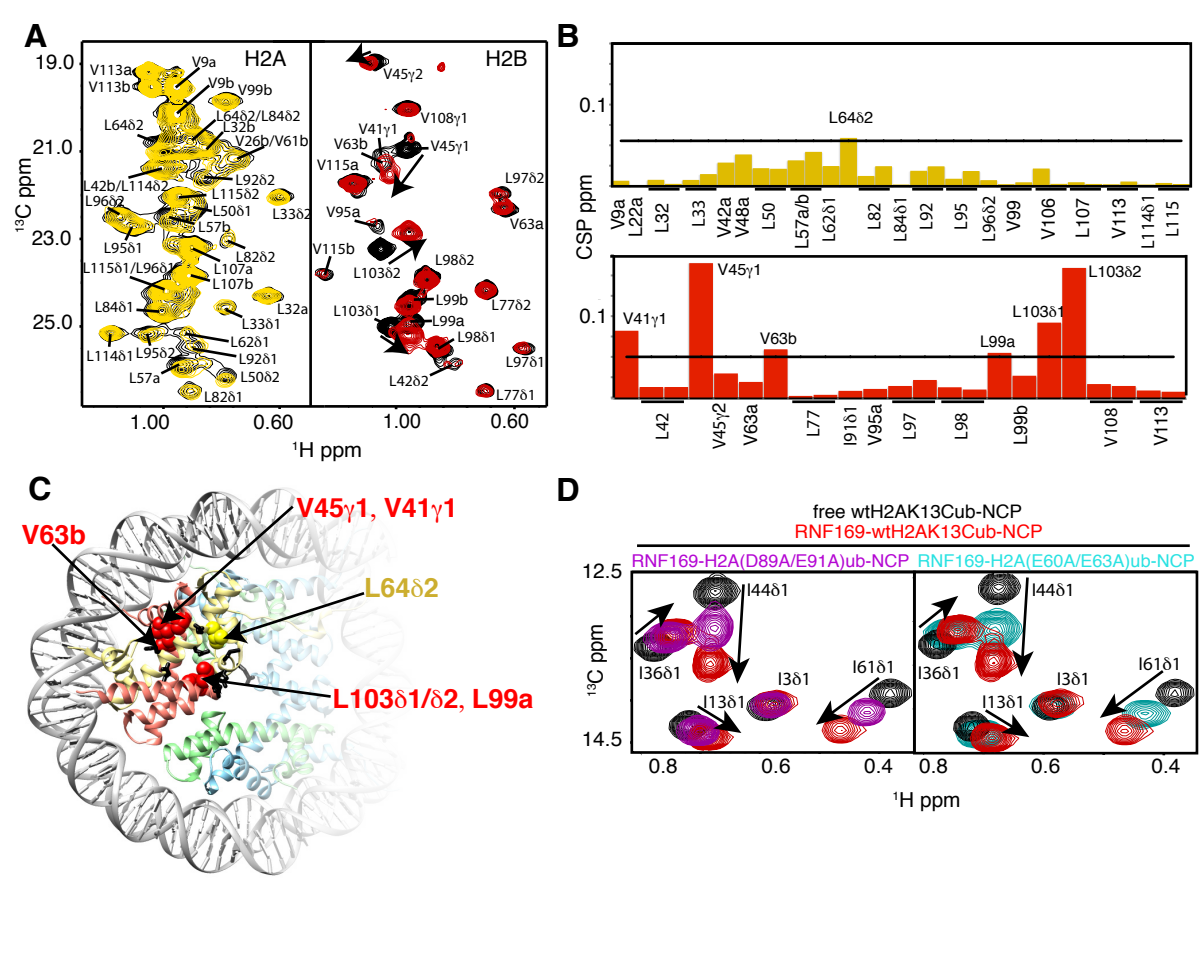
A
H2A
H2B
^{13}C ppm
^{1}H ppm
B
CSP ppm
C
V63b
V45γ1, V41γ1
L64δ2
L103δ1/δ2, L99a
D
free wtH2AK13Cub-NCP
RNF169-wtH2AK13Cub-NCP
RNF169-H2A(D89A/E91A)ub-NCP
RNF169-H2A(E60A/E63A)ub-NCP
^{13}C ppm
^{1}H ppm

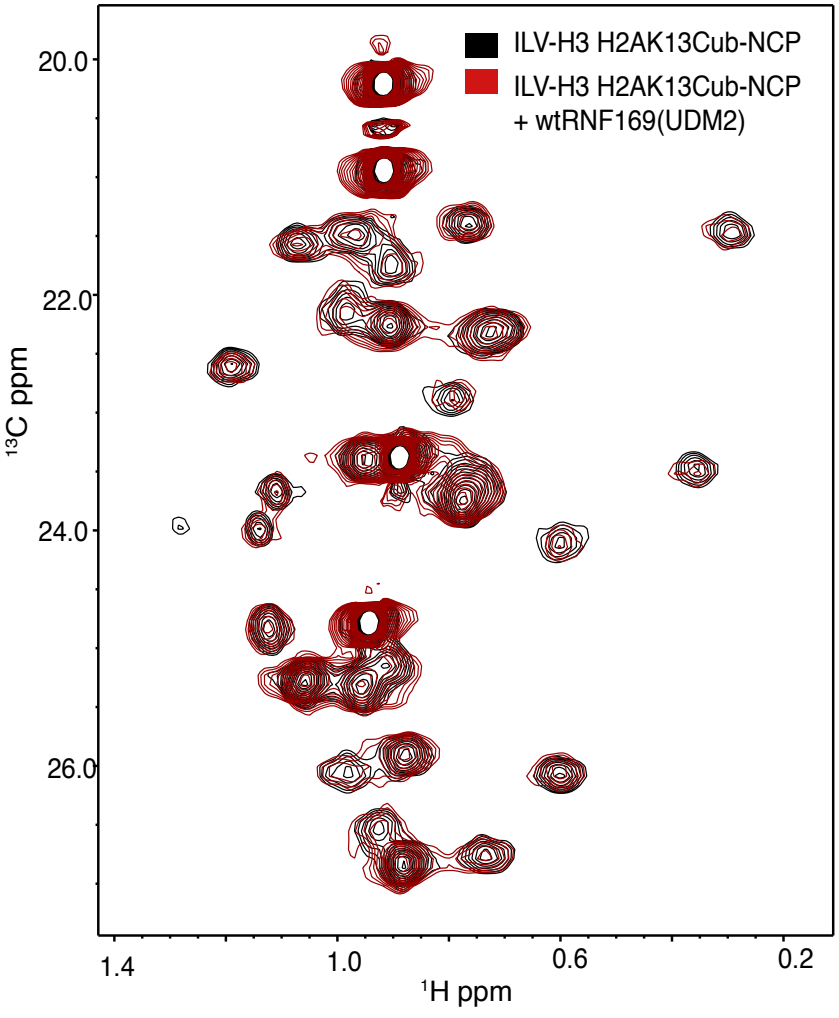
ILV-H3 H2AK13Cub-NCP
ILV-H3 H2AK13Cub-NCP
+ wtRNF169(UDM2)
20.0
22.0
24.0
26.0
^{13}C ppm
1.4
1.0
0.6
0.2
^{1}H ppm

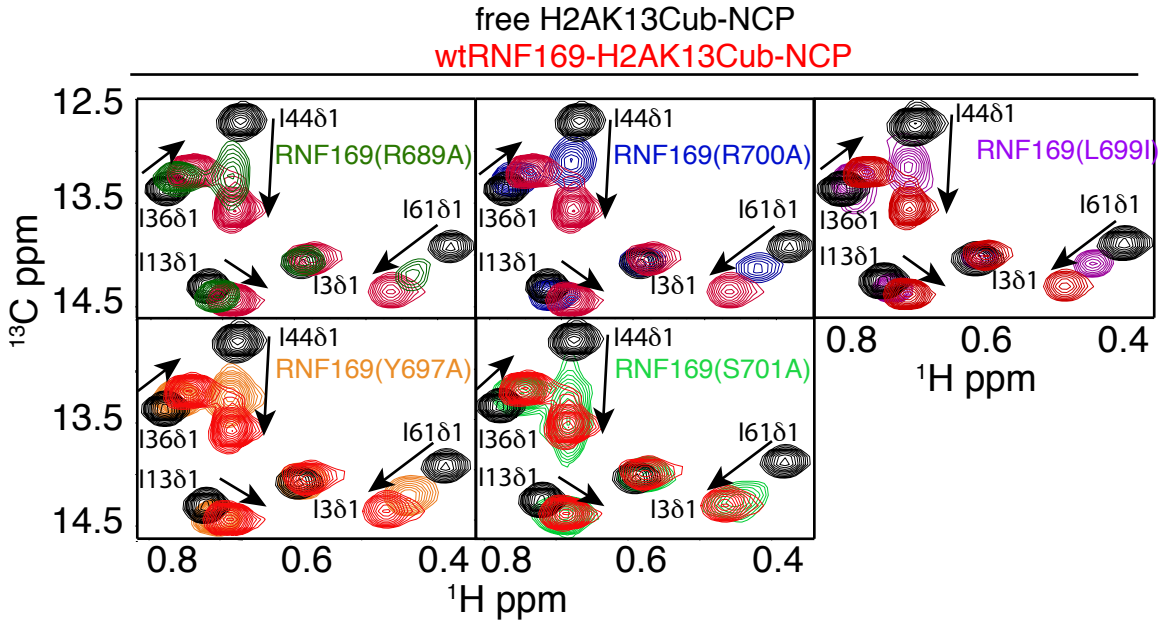
free H2AK13Cub-NCP
wtRNF169-H2AK13Cub-NCP
I44δ1
RNF169(R689A)
I36δ1
I13δ1
I61δ1
I3δ1
I44δ1
RNF169(R700A)
I36δ1
I13δ1
I61δ1
I3δ1
I44δ1
RNF169(L699I)
I36δ1
I13δ1
I61δ1
I3δ1
I44δ1
RNF169(Y697A)
I36δ1
I13δ1
I61δ1
I3δ1
I44δ1
RNF169(S701A)
I36δ1
I13δ1
I61δ1
I3δ1
12.5
13.5
14.5
13.5
14.5
^{13}C ppm
0.8
0.6
0.4
0.8
0.6
0.4
0.8
0.6
0.4
^{1}H ppm

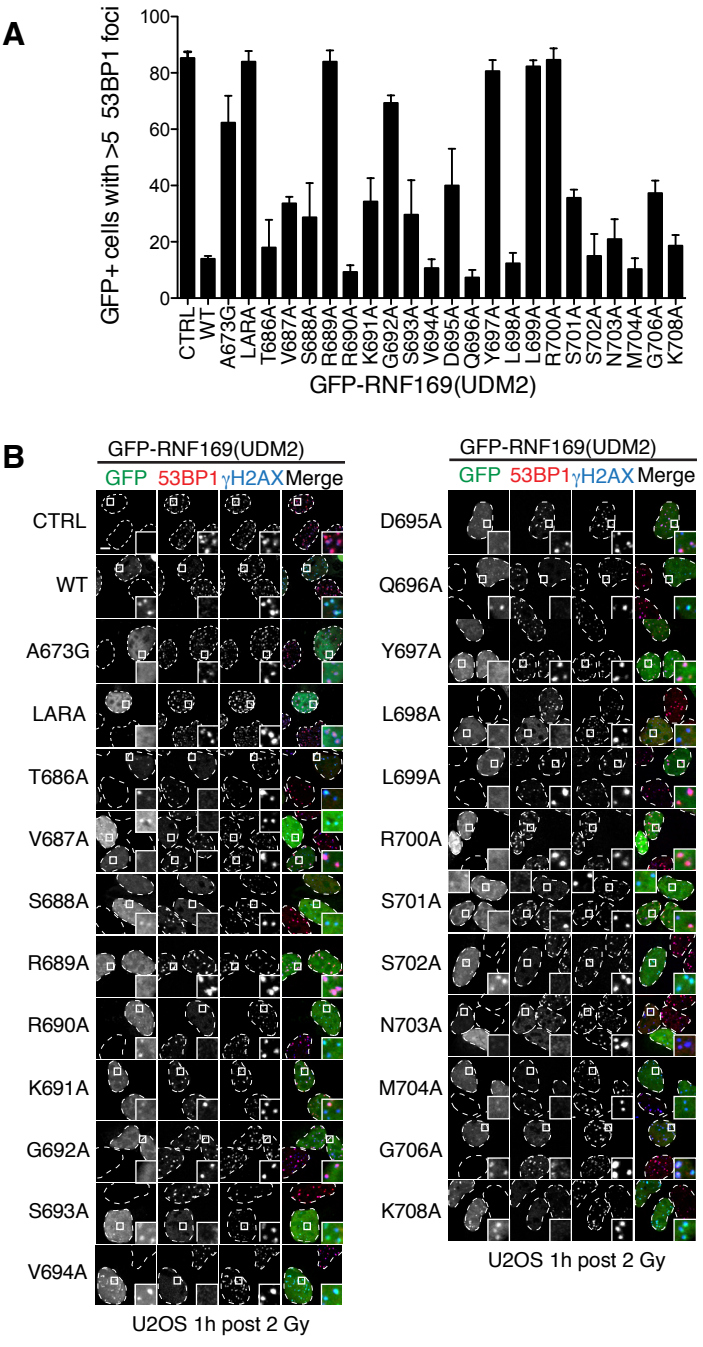
A
GFP+ cells with >5 53BP1 foci
100
80
60
40
20
0
CTRL
WT
A673G
LARA
T686A
V687A
S688A
R689A
R690A
K691A
G692A
S693A
V694A
D695A
Q696A
Y697A
L698A
L699A
R700A
S701A
S702A
N703A
M704A
G706A
K708A
GFP-RNF169(UDM2)
B
GFP-RNF169(UDM2)
GFP 53BP1 γH2AX Merge
CTRL
WT
A673G
LARA
T686A
V687A
S688A
R689A
R690A
K691A
G692A
S693A
V694A
U2OS 1h post 2 Gy
GFP-RNF169(UDM2)
GFP 53BP1 γH2AX Merge
D695A
Q696A
Y697A
L698A
L699A
R700A
S701A
S702A
N703A
M704A
G706A
K708A
U2OS 1h post 2 Gy

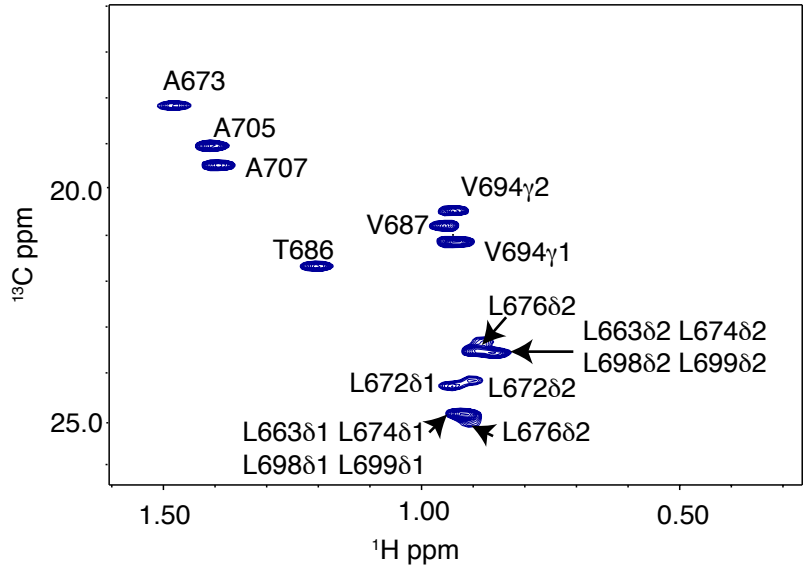
A673
A705
A707
V694γ2
V687
T686
V694γ1
L676δ2
L663δ2 L674δ2
L698δ2 L699δ2
L672δ1
L672δ2
L663δ1 L674δ1
L676δ2
L698δ1 L699δ1
20.0
25.0
^{13}C ppm
1.50
1.00
0.50
^{1}H ppm

A

LRM2

RNF169 689 RRKGSVDQYLLRSSNMAGAK 708

LANA 1 MAPPGMRLRSGRSTGAP 17

B

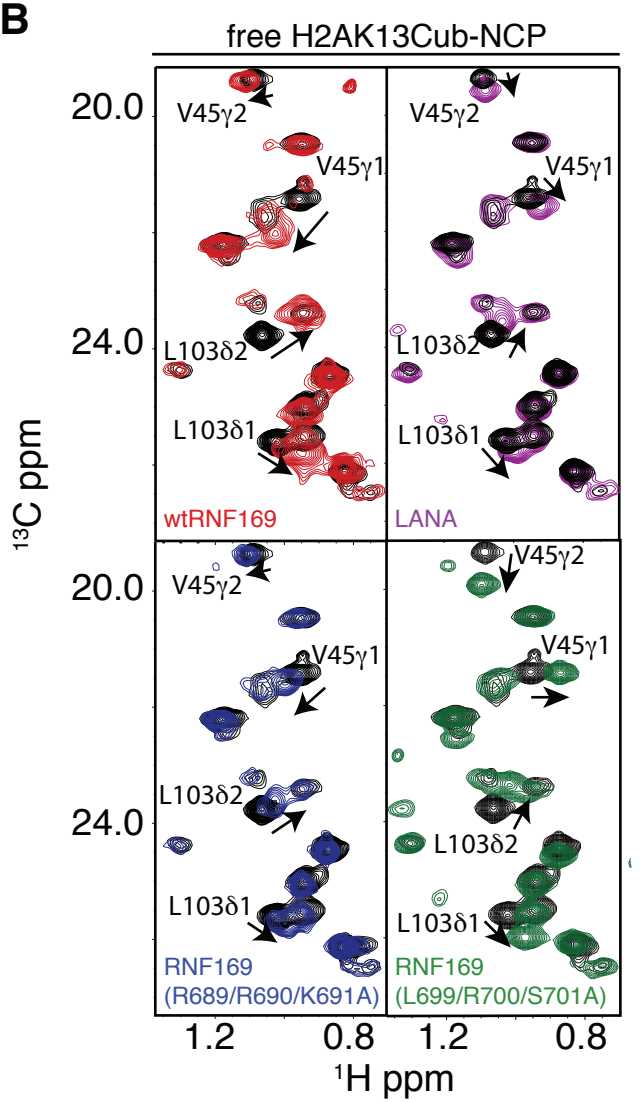

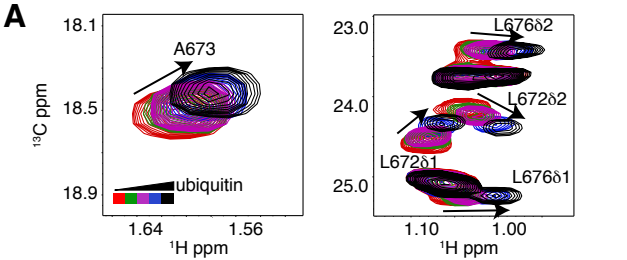
A
18.1
18.5
18.9
^{13}C ppm
A673
ubiquitin
1.64
1.56
^{1}H ppm
23.0
24.0
25.0
L676δ2
L672δ2
L672δ1
L676δ1
1.10
1.00
^{1}H ppm

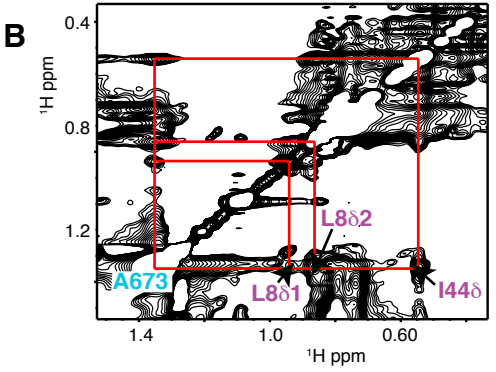
B
0.4
0.8
1.2
^{1}H ppm
L8δ2
A673
L8δ1
I44δ
1.4
1.0
0.60
^{1}H ppm

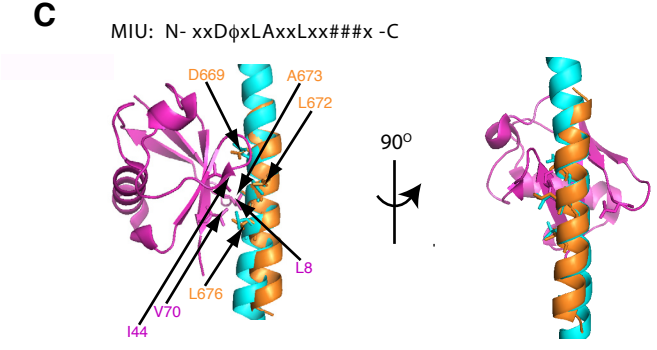
C
MIU: N- xxDϕxLAxxLxx###x -C
D669
A673
L672
L8
L676
V70
I44
90°

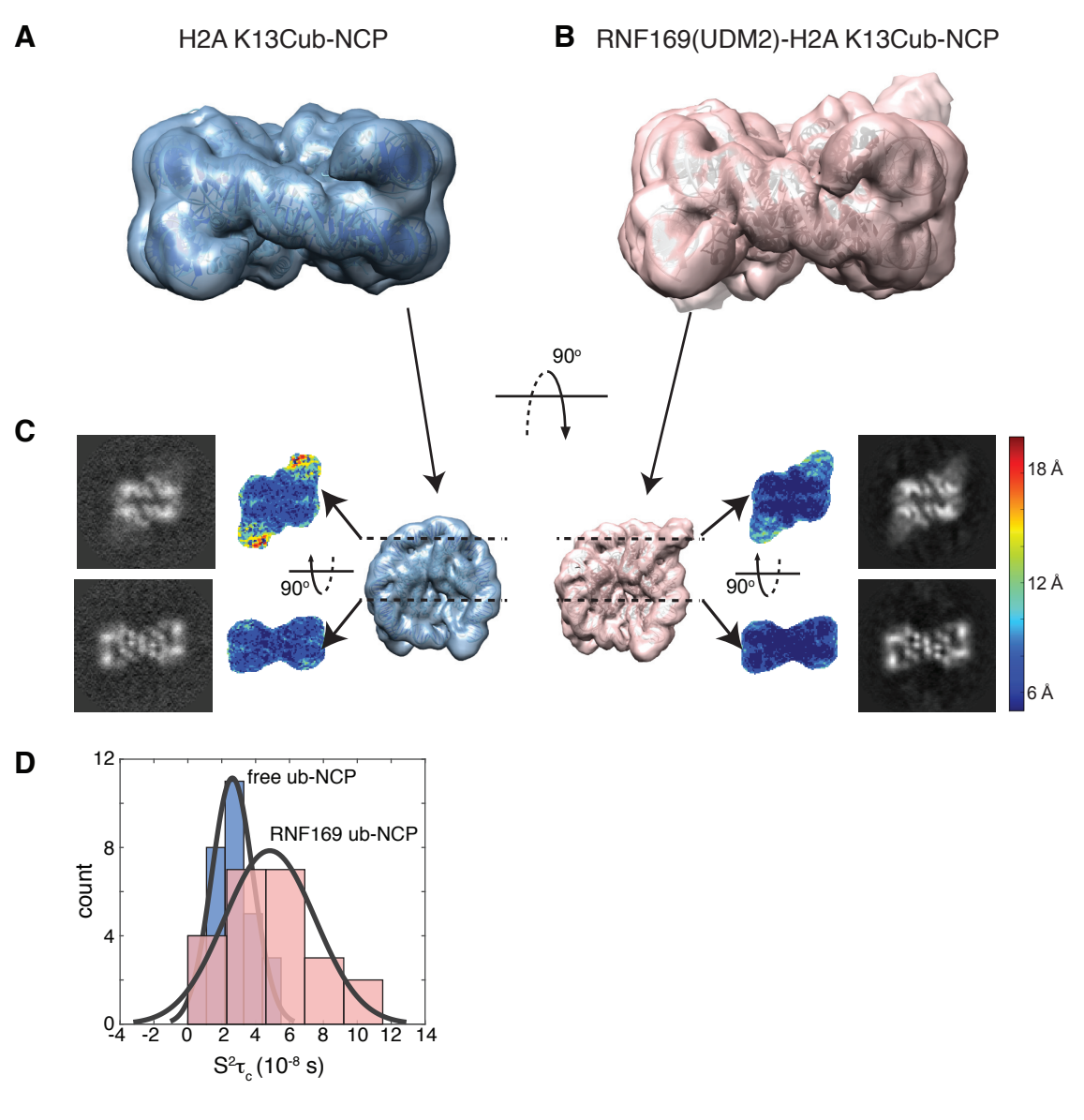
A
H2A K13Cub-NCP
B
RNF169(UDM2)-H2A K13Cub-NCP
90°
C
90°
90°
18 Å
12 Å
6 Å
D
free ub-NCP
RNF169 ub-NCP
count
12
8
4
0
-4
-2
0
2
4
6
8
10
12
14
S²τc (10⁻⁸ s)

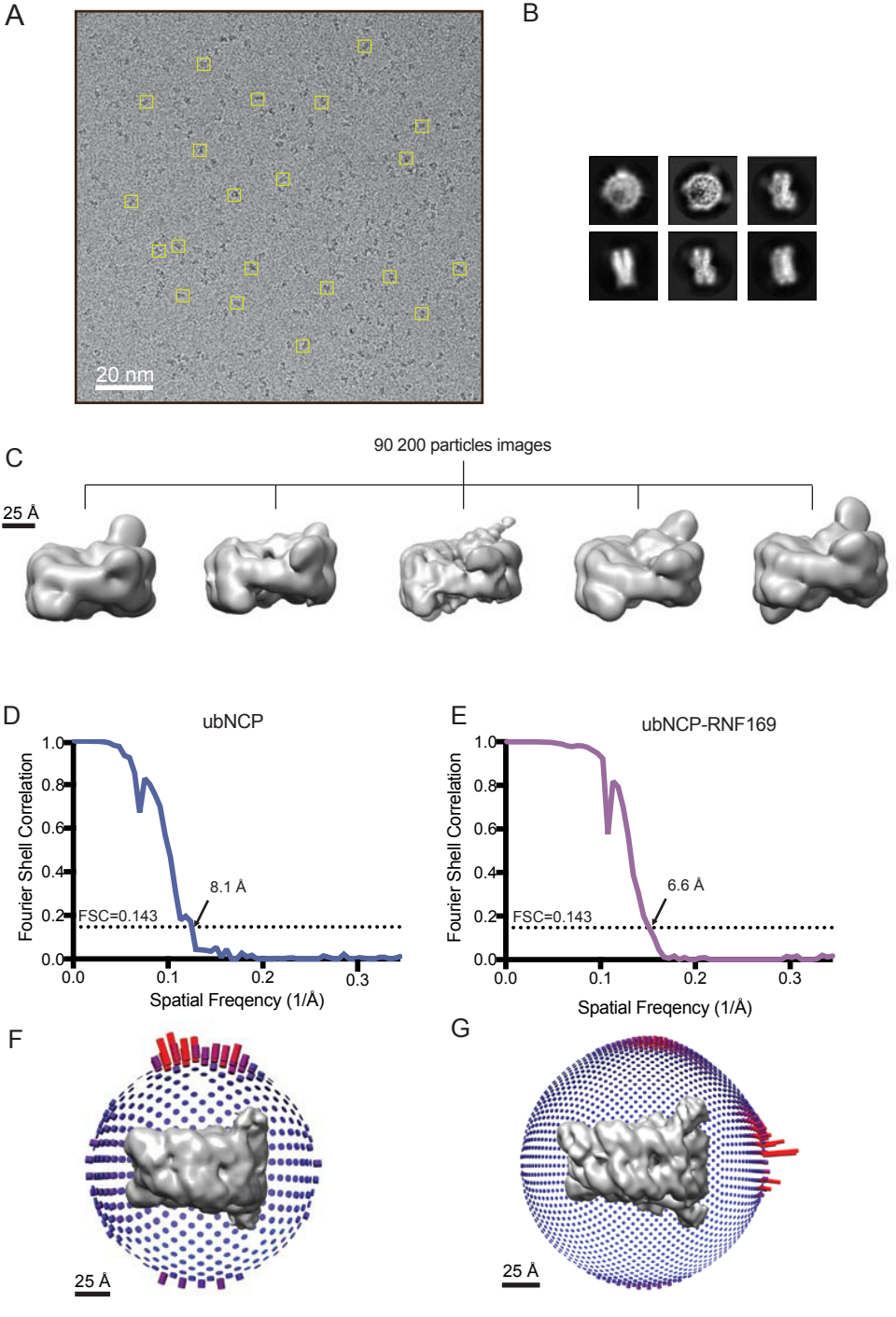
A
20 nm
B
C
90 200 particles images
25 Å
D
ubNCP
Fourier Shell Correlation
1.0
0.8
0.6
0.4
0.2
0.0
8.1 Å
FSC=0.143
0.0
0.1
0.2
0.3
Spatial Freqency (1/Å)
E
ubNCP-RNF169
Fourier Shell Correlation
1.0
0.8
0.6
0.4
0.2
0.0
6.6 Å
FSC=0.143
0.0
0.1
0.2
0.3
Spatial Freqency (1/Å)
F
25 Å
G
25 Å

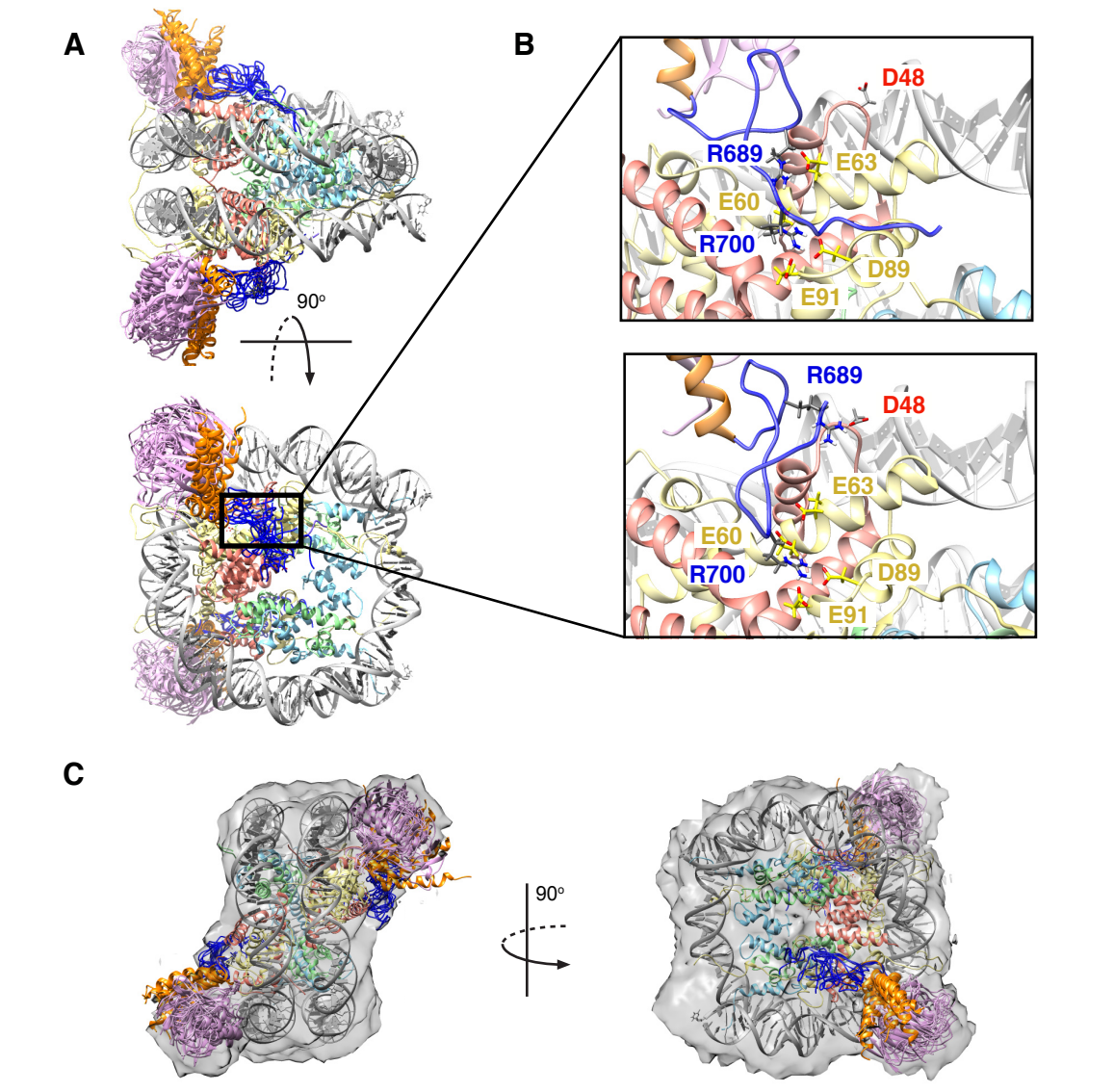
A
B
C
90°
D48
R689
E63
E60
R700
D89
E91
R689
D48
E63
E60
R700
D89
E91
90°

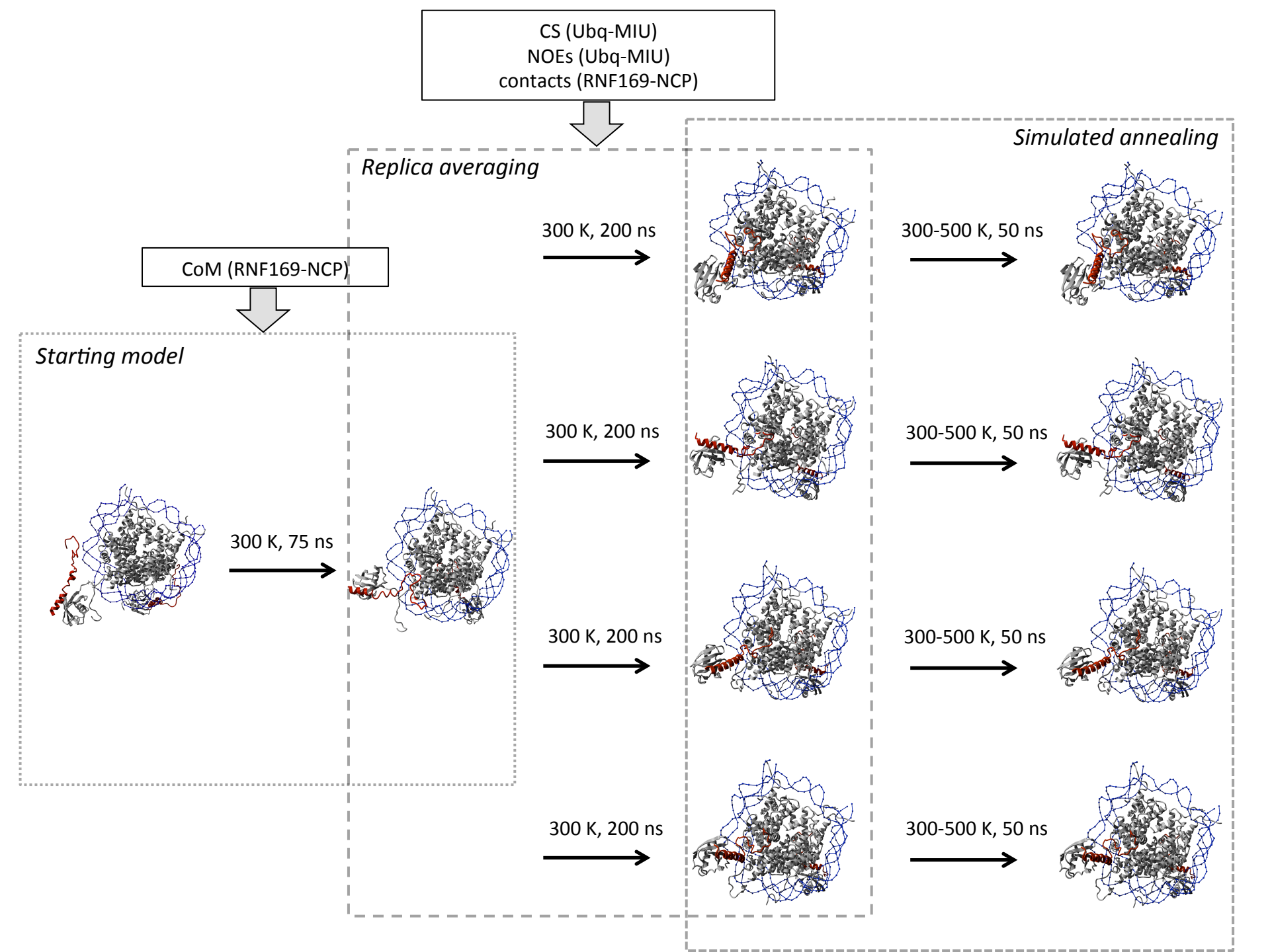
CS (Ubq-MIU)
NOEs (Ubq-MIU)
contacts (RNF169-NCP)
Simulated annealing
Replica averaging
300 K, 200 ns
300-500 K, 50 ns
CoM (RNF169-NCP)
Starting model
300 K, 200 ns
300-500 K, 50 ns
300 K, 75 ns
300 K, 200 ns
300-500 K, 50 ns
300 K, 200 ns
300-500 K, 50 ns

A

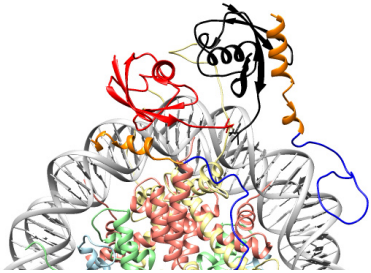

B